

ABSTRACT

FULLER, JOHN DAVID. Methods to Alleviate Processing Requirements of High-Fidelity Multibody Parachute Simulations Involving a Confluence Mass. (Under the direction of Dr. Robert H. Tolson.)

Methods designed to reduce the numerical stiffness and processing requirements of high fidelity entry trajectory models involving parachutes are explored. Parachute deployment systems have often been simulated using rigid body dynamic models. The system is comprised of a parachute rigid body attached to the vehicle via a confluence mass with flexible lines. The simulations incorporating the confluence mass often take excessive amounts of processing time due to the relatively small mass of the confluence point and the resulting high frequency motion. The two methods investigated here seek to simplify the equations of motion to be integrated in the simulation, removing the numerical stiffness and increasing the required time step.

Initially an analytic solution is derived from previous work on the subject and is used to linearize the confluence point equations of motion about an equilibrium point. The motion of the confluence point about the equilibrium point can then be reduced to that of a simple harmonic oscillator, resolved analytically and averaged over a larger time step than required for integration of the original set of equations of motion. This procedure allows the removal of the equations of motion of the confluence mass from the system, replacing them with analytic solutions for its position and velocity. The numerically stiff portion of the simulation is thus removed, significantly improving processing time.

The second method developed is entitled the singular perturbation method, and involves suppressing the small inertia of the confluence mass responsible for high frequency motion. The singularly perturbed system allows simplification of the equations of motion by removing the confluence point velocity state equations. The velocity state vector may be estimated by taking the limit of the equations of motion of the confluence point as its mass approaches zero. The stiffness of

the equations is again removed, thereby increasing the integration time step and decreasing overall processing time. The singular perturbation method is applied to parachute entry models of the Mars Exploration Rover mission as well as the Crew Exploration Vehicle abort mode.

Results from both methods are compared to models in which a confluence point with mass is used with integration of the full set of equations of motion. Performance is evaluated in each case by way of comparing integration time step to measure the benefits of application of the methods. Necessary assumptions and the resulting implications for each approach are defined and evaluated to assess the convenience and application of the methods.

Methods to Alleviate Processing Requirements of High-Fidelity Multibody
Parachute Simulations Involving a Confluence Mass

by
John David Fuller

A thesis submitted to the Graduate Faculty of
North Carolina State University
in partial fulfillment of the
requirements for the Degree of
Master of Science

Aerospace Engineering

Raleigh, North Carolina

2009

APPROVED BY:

Dr. Fred DeJarnette

Dr. John Franke

Dr. Robert Tolson
Chair of Advisory Committee

DEDICATION

This work is dedicated to my mother, whose continuing support
has sustained me on my journey through life.

BIOGRAPHY

John Fuller obtained a Bachelor of Science degree in Aerospace Engineering from North Carolina State University in 2006. Following graduation, he enrolled in the Graduate School of NC State University and began research at NASA Langley Research Center in Hampton, Virginia under the direction of Dr. Robert Tolson. Here he performed tasks for the Atmospheric Flight Entry Systems Branch assisting in analyses with the Crew Exploration Vehicle for pad abort simulations. He also developed a standalone free-molecular analysis tool for aerobraking spacecraft called FreeMat. His other work includes trajectory analyses for the Lunar Lander Preparatory Study. John earned his private pilot's license at Langley Air Force Base in 2008. He has been and always will remain fascinated by all machines designed to take flight and leave this Earth.

ACKNOWLEDGEMENTS

I would like to acknowledge several associates with vital roles in the development of this research. Dr. Robert Tolson has provided invaluable guidance without which this work would not have been possible. I believe I am a better person after having worked with him for the past two years. I thank Dr. Fred DeJarnette for his role in guiding me in both undergraduate and graduate endeavors, as well as helping in the transition between the two periods. I would also like to thank Langley aerospace engineers Daniel Litton, Ben Raiszadeh, and Jeremy Shidner for their continued assistance and support. Finally, I am gracious to both NASA and the National Institute of Aerospace for the outstanding opportunity for research they have provided me, and will continue to provide to countless other graduate students in this field.

TABLE OF CONTENTS

LIST OF TABLES	vi
LIST OF FIGURES	vii
LIST OF SYMBOLS.....	viii
1 Introduction.....	1
1.1 Problem Statement.....	1
1.2 Model Configuration	3
1.3 Methodology	4
2 Analytic Confluence Solution.....	6
2.1 Theory	6
2.2 Validation	9
2.3 Discussion	15
3 Singular Perturbation Method.....	18
3.1 Theory	18
3.2 Validation	23
3.2.1 Mars Exploration Rover Simulation.....	24
3.2.2 Crew Exploration Vehicle Simulation.....	45
3.3 Discussion	52
4 Conclusions.....	54
References	56
Appendices	57

LIST OF TABLES

Table 2.1 Simple model specifications.....	9
Table 2.2 Linearized case equivalent parameters.....	10
Table 2.3 Confluence initial conditions.....	11
Table 3.1 MER model line properties	24
Table 3.2 MER model mass properties	24
Table 3.3 Mars planet model parameters.....	25
Table 3.4 MER test case 1 initial conditions.....	28
Table 3.5 MER test case 2 initial conditions.....	29
Table 3.6 MER test case 3 initial conditions.....	31
Table 3.7 MER test case 4 initial conditions.....	35
Table 3.8 MER test case 5 and 6 initial conditions.....	38
Table 3.9 Pad Abort 1 event log.....	46

LIST OF FIGURES

Fig. 1.1 Generic rigid body parachute model with confluence mass.....	2
Fig. 1.2 Confluence point free body diagram.....	3
Fig. 2.1 Simple confluence motion model.....	9
Fig. 2.2 Confluence analytic position with respect to equilibrium point.....	12
Fig. 2.3 Analytic and integrated comparison of confluence position	14
Fig. 3.1 MER descent configuration.....	24
Fig. 3.2 MER body axes and bridle attachment points.....	25
Fig. 3.3 Mars atmospheric density profile.....	26
Fig. 3.4 MER zero trim parachute model	27
Fig. 3.5 Test case 1 tension history of bridles	28
Fig. 3.6 Test case 2 tension history of bridles	30
Fig. 3.7 Test case 2 tension history of riser.....	30
Fig. 3.8 Test case 3 tension history of bridle 1.....	32
Fig. 3.9 Test case 3 tension history of bridle 3.....	32
Fig. 3.10 Test case 3 tension history of riser	33
Fig. 3.11 Test case 3 confluence point lateral velocity	34
Fig. 3.12 Test case 4 tension history of bridle 1.....	35
Fig. 3.13 Test case 4 tension history of bridle 2.....	35
Fig. 3.14 Test case 4 tension history of bridle 3.....	36
Fig. 3.15 Test case 4 confluence point lateral velocity	37
Fig. 3.16 Test case 5 tension history of bridles 1 and 2	38
Fig. 3.17 Test case 5 tension history of bridle 3.....	38
Fig. 3.18 Test case 5 tension history of riser.....	39
Fig. 3.19 Test case 5 confluence point lateral velocity	40
Fig. 3.20 Test case 6 tension history of bridle 1.....	42
Fig. 3.21 Test case 6 tension history of bridle 2.....	42
Fig. 3.22 Test case 6 tension history of bridle 3.....	43
Fig. 3.23 Test case 6 confluence point lateral velocity	44
Fig. 3.24 CEV Pad Abort 1 test scenario.....	46
Fig. 3.25 Pad Abort 1 tension history of bridle 1	47
Fig. 3.26 Pad Abort 1 tension history of bridle 2	48
Fig. 3.27 Pad Abort 1 tension history of bridle 3	48
Fig. 3.28 Pad Abort 1 confluence point relative velocity (CEV body frame)	49
Fig. 3.29 Pad Abort 1 CEV Euler orientation angles	51

LIST OF SYMBOLS

C	damping coefficient
C_c	confluence point damping coefficient
C_N	parachute normal force coefficient
\vec{F}_d	confluence point damping force
\vec{F}_{ext}	external force vector on parachute or vehicle
\vec{g}	acceleration vector due to gravity
I_p	parachute/entrained air mass inertia tensor
I_v	vehicle inertia tensor
K	stiffness coefficient
$L_{0,i}$	unstretched length of line i
L_i	length of line i
\vec{M}_{ext}	external moment vector on parachute or vehicle
\vec{M}_i	moment vector imparted by line i
m_c	confluence point mass
m_p	parachute/entrained air mass
m_v	vehicle mass
\hat{n}_i	unit vector of line i
n_{ix}	x component of \hat{n}_i
n_{iy}	y component of \hat{n}_i
n_{iz}	z component of \hat{n}_i
R_e	elliptical planet equatorial radius
R_p	elliptical planet polar radius
\vec{r}_{eq}	inertial position vector of confluence equilibrium point
\vec{v}_{eq}	inertial velocity vector of confluence equilibrium point
\vec{r}_c	inertial position vector of confluence point
\vec{v}_c	inertial velocity vector of confluence point
\vec{a}_c	inertial acceleration vector of confluence point
\vec{r}_i	inertial position vector of line i attach point
\vec{v}_i	inertial velocity vector of line i attach point
\vec{a}_p	inertial acceleration vector of parachute
\vec{a}_v	inertial acceleration vector of vehicle
T	oscillation period
\vec{T}_i	tension in line i
κ	condition number
μ	planet gravitational constant
ξ	damping ratio
Ω	planet rotation rate
ω_n	natural frequency
$\vec{\omega}_p$	body rotation rate vector of parachute
$\vec{\omega}_v$	body rotation rate vector of vehicle
$\vec{\dot{\omega}}_p$	body angular acceleration vector of parachute
$\vec{\dot{\omega}}_v$	body angular acceleration vector of vehicle

1 Introduction

1.1 Problem Statement

Many planetary entry systems employ a parachute system in the latter phases of entry, descent, and landing. Trajectory analysis programs often model these systems using 6 degree-of-freedom motion of multiple rigid bodies¹⁻⁷. The parachute and vehicles are modeled as individual rigid bodies connected by flexible lines. To more realistically model the system, a confluence point is used between the bodies where the lines converge. Generally the confluence point is modeled as an individual, 3 degree-of-freedom body. An example configuration is shown in Fig. 1.1. The solution to the differential equations of the confluence point is on a different time scale than those of the more massive bodies of the system. Provided that the confluence point mass is much smaller than the masses of the parachute and the vehicle, the high frequency motion of this mass requires a small time step to integrate the equations of motion. Some trajectory analysis software packages solve the differential equations of motion simultaneously with a constant time step integrator. The small time step required for the integration of the acceleration of the confluence point is the limiting factor of the entire simulation. Increasing this time step would greatly reduce the turn-around time of trajectory simulations involving parachute deployment with a confluence point.

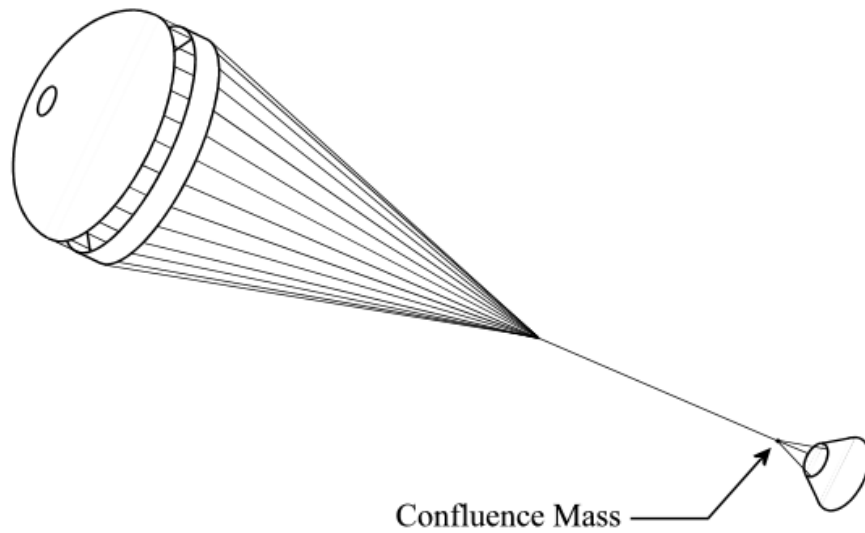


Fig. 1.1 Generic rigid body parachute model with confluence mass

Trajectory analysts are more concerned with the behavior of the parachute and attached bodies rather than the behavior of the confluence point. The overall motion of the more massive bodies is generally unaffected by the small inertias of the confluence point mass. The primary goal would be to eliminate the confluence point mass while still modeling the system dynamics as a result of the lines converging at that point. The scope of this work is to explore different methods of circumventing integration of the confluence point equations of motion while retaining the prediction of the dynamics of the system.

1.2 Model Configuration

The particular system modeled for this method is comprised of a rigid body parachute connected to a rigid body vehicle by way of a confluence point. The parachute is connected to the confluence point by a single riser, and the confluence point has three bridles that connect to the vehicle. The parachute and vehicle are modeled as 6 degrees-of-freedom bodies, while the confluence point is a 3 degrees-of-freedom body. The free body diagram of the confluence point is shown in Fig. 1.2. Assuming the confluence point has a mass of m_c , the equations of motion of the entire system are

$$m_v \ddot{\vec{r}}_v = \vec{F}_{ext,v} + m_v \vec{g} - (\vec{T}_1 + \vec{T}_2 + \vec{T}_3) \quad (1.1)$$

$$\boxed{m_c \ddot{\vec{r}}_c = \vec{T}_1 + \vec{T}_2 + \vec{T}_3 + \vec{T}_4 + m_c \vec{g}} \quad (1.2)$$

$$m_p \ddot{\vec{r}}_p = \vec{F}_{ext,p} + m_p \vec{g} - \vec{T}_4 \quad (1.3)$$

$$\ddot{\vec{\omega}}_v = [I_v]^{-1} \{ \vec{M}_{ext,v} - \vec{M}_1 - \vec{M}_2 - \vec{M}_3 - \vec{\omega}_v \times [I_v] \cdot \vec{\omega}_v \} \quad (1.4)$$

$$\ddot{\vec{\omega}}_p = [I_p]^{-1} \{ \vec{M}_{ext,p} - \vec{M}_4 - \vec{\omega}_p \times [I_p] \cdot \vec{\omega}_p \} \quad (1.5)$$

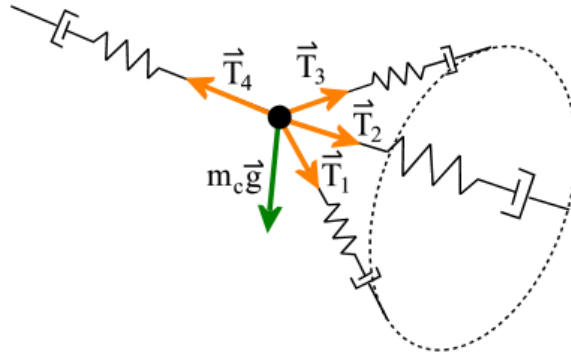


Fig. 1.2 Confluence point free body diagram

The parachute and vehicle are subject to gravity, as well as aerodynamic forces and moments denoted by the subscript “ext.” Equation 1.2 is on a different time scale than the other equations of motion, resulting in the numerically stiff problem. The bridles and riser are modeled as springs with stiffness and damping values defined by the user. The tension of each line is defined as

$$\vec{T}_i = [K_i(\|\vec{r}_i - \vec{r}_c\| - L_{0,i}) + C_i(\dot{\vec{r}}_i - \dot{\vec{r}}_c) \cdot \hat{n}_i] \hat{n}_i \quad (1.6)$$

where

$$\hat{n}_i = \frac{(\vec{r}_i - \vec{r}_c)}{\|\vec{r}_i - \vec{r}_c\|} \quad (1.7)$$

Note that no compressive forces are permitted in the lines for any of this work. Most models of this nature incorporate extremely high stiffness values, due to the use of Kevlar lines. Higher spring stiffness values increase the numerical stiffness of the problem. Some models incorporate very little damping to maintain conservative estimations in capsule swing and coning, which will be addressed in each approach.

1.3 Methodology

Research at NASA Langley briefly investigated the problems with confluence point mass integration with interesting results. Past approaches⁷ included an equilibrium point solution in which the confluence point is placed at an equilibrium location based only on line tension, i.e. at each time step the confluence point is in static equilibrium. The equations of motion for the confluence mass were eliminated from the simulation entirely. A further investigation of the equilibrium point and its usefulness in predicting the confluence point motion is warranted. An analytic solution is developed from linearization of the confluence point equations of motion, evaluated at the equilibrium point. This analytic solution was devised once observations of the system indicated that the confluence point oscillates about the equilibrium point at a different frequency in each axis. Assumptions of small

deflections in the confluence point from equilibrium allow linearization of the coupled, non-linear equations of motion.

The analytic solution is applied to a system similar to the configuration in Fig. 1.1, where the attachment points are held at fixed locations. The confluence point is then deflected from equilibrium and the resulting motion is predicted and compared against full integration of the equations of motion at significantly lower processing costs. Difficulties can arise in the analytic solution in the form of non-convergence of the Newton iterative solver. Consequently, development of a new method without the hindrance of iterative solutions is desired. The singular perturbation method employs the idea of the equilibrium point solution but instead uses the fundamental equilibrium equation to solve for the confluence point inertial velocity. The result is a reduced first order differential equation in terms of position and velocity of the confluence point. The velocity is integrated to determine the inertial position of the confluence point. The high frequency motion of the confluence point is eliminated and the required time step for the simulation can be increased by two orders of magnitude. Implications of the singular perturbation method include the investigation and handling of slack cases, when one of the connecting lines has no tension. This requires the use of damping on the confluence point, a standard practice in parachute system models.

The singular perturbation method is applied to models of the Mars Exploration Rover (MER) entry configuration as well as the Crew Exploration Vehicle (CEV) abort mode configuration. The models are analyzed using POSTII, a trajectory analysis program used to simulate entry, descent, and landing scenarios⁸. Results from the models using a point mass at the confluence point is compared to results using the singular method. The MER model is used in several simple free-fall cases with varying initial conditions. The CEV abort mode configuration utilizes two sequentially-timed parachute systems with confluence points. The method is applied to both systems in the same abort scenario and initialized following the abort tower jettison event.

2 Analytic Confluence Solution

2.1 Theory

Study of the confluence point in this system reveals particular inherent behavior with respect to the equilibrium point. The equilibrium point is the location at which the confluence point would be located in static equilibrium. As a result, a perturbation of the confluence point from equilibrium results in harmonic oscillation about this equilibrium point in the three axes. This motion is a function of the magnitude of the perturbation, as well as the stiffness and damping properties of the connecting lines. Given these observations, an analytic solution based on a simple harmonic oscillator is conceivable. Linearization of the confluence point mass equations about the equilibrium point provides the analytic solution, developed here. The procedure to locate the equilibrium point is further explained in the references⁷.

The equations of motion for the confluence mass in condensed form are

$$m_c \ddot{\vec{r}}_c - \sum_{i=1}^4 [K_i (\|\vec{r}_i - \vec{r}_c\| - L_{0,i}) + C_i (\dot{\vec{r}}_i - \dot{\vec{r}}_c) \cdot \hat{n}_i] \hat{n}_i = 0 \quad (2.1)$$

Separating the equations into the three axes and expanding provides

$$f_x = m_c \ddot{r}_{cx} - \sum_{i=1}^4 K_i n_{ix} \left(\sqrt{(\dot{r}_{ix} - \dot{r}_{cx})^2 + (\dot{r}_{iy} - \dot{r}_{cy})^2 + (\dot{r}_{iz} - \dot{r}_{cz})^2} - L_{0,i} \right) - \sum_{i=1}^4 C_i \{ (\dot{r}_{ix} - \dot{r}_{cx}) n_{ix}^2 + (\dot{r}_{iy} - \dot{r}_{cy}) n_{ix} n_{iy} + (\dot{r}_{iz} - \dot{r}_{cz}) n_{ix} n_{iz} \} = 0 \quad (2.2)$$

$$f_y = m_c \ddot{r}_{cy} - \sum_{i=1}^4 K_i n_{iy} \left(\sqrt{(\dot{r}_{ix} - \dot{r}_{cx})^2 + (\dot{r}_{iy} - \dot{r}_{cy})^2 + (\dot{r}_{iz} - \dot{r}_{cz})^2} - L_{0,i} \right) - \sum_{i=1}^4 C_i \{ (\dot{r}_{ix} - \dot{r}_{cx}) n_{ix} n_{iy} + (\dot{r}_{iy} - \dot{r}_{cy}) n_{iy}^2 + (\dot{r}_{iz} - \dot{r}_{cz}) n_{iy} n_{iz} \} = 0 \quad (2.3)$$

$$f_z = m_c \ddot{r}_{cz} - \sum_{i=1}^4 K_i n_{iz} \left(\sqrt{(\dot{r}_{ix} - \dot{r}_{cx})^2 + (\dot{r}_{iy} - \dot{r}_{cy})^2 + (\dot{r}_{iz} - \dot{r}_{cz})^2} - L_{0,i} \right) - \sum_{i=1}^4 C_i \{ (\dot{r}_{ix} - \dot{r}_{cx}) n_{ix} n_{iy} + (\dot{r}_{iy} - \dot{r}_{cy}) n_{iy} n_{iz} + (\dot{r}_{iz} - \dot{r}_{cz}) n_{iz}^2 \} = 0 \quad (2.4)$$

Linearization of f_x about the equilibrium point is defined by

$$\begin{aligned} & \left. \frac{\partial f_x}{\partial \dot{r}_{cx}} \right|_{eq} \Delta \dot{r}_{cx} + \left. \frac{\partial f_x}{\partial \dot{r}_{cy}} \right|_{eq} \Delta \dot{r}_{cy} + \left. \frac{\partial f_x}{\partial \dot{r}_{cz}} \right|_{eq} \Delta \dot{r}_{cz} \\ & + \left. \frac{\partial f_x}{\partial r_{cx}} \right|_{eq} \Delta r_{cx} + \left. \frac{\partial f_x}{\partial r_{cy}} \right|_{eq} \Delta r_{cy} + \left. \frac{\partial f_x}{\partial r_{cz}} \right|_{eq} \Delta r_{cz} = 0 \end{aligned} \quad (2.5)$$

Linearizing f_y and f_z as well and rewriting in matrix format provides a simple, damped harmonic oscillator equation

$$m_c [I]_{3 \times 3} \Delta \ddot{\vec{r}}_c + \bar{C} \Delta \dot{\vec{r}}_c + \bar{K} \Delta \vec{r}_c = 0 \quad (2.6)$$

where

$$\Delta \vec{r}_c = \vec{r}_c - \vec{r}_{eq}$$

$$\Delta \dot{\vec{r}}_c = \dot{\vec{r}}_c - \dot{\vec{r}}_{eq}$$

and \bar{C} and \bar{K} are the linearized equivalent damping and stiffness matrices, respectively.

These matrices are defined as

$$\bar{C} = \begin{bmatrix} \frac{\partial f_x}{\partial \dot{r}_{cx}} & \frac{\partial f_x}{\partial \dot{r}_{cy}} & \frac{\partial f_x}{\partial \dot{r}_{cz}} \\ \frac{\partial f_y}{\partial \dot{r}_{cx}} & \frac{\partial f_y}{\partial \dot{r}_{cy}} & \frac{\partial f_y}{\partial \dot{r}_{cz}} \\ \frac{\partial f_z}{\partial \dot{r}_{cx}} & \frac{\partial f_z}{\partial \dot{r}_{cy}} & \frac{\partial f_z}{\partial \dot{r}_{cz}} \end{bmatrix}_{r_c=r_{eq}} \quad \bar{K} = \begin{bmatrix} \frac{\partial f_x}{\partial r_{cx}} & \frac{\partial f_x}{\partial r_{cy}} & \frac{\partial f_x}{\partial r_{cz}} \\ \frac{\partial f_y}{\partial r_{cx}} & \frac{\partial f_y}{\partial r_{cy}} & \frac{\partial f_y}{\partial r_{cz}} \\ \frac{\partial f_z}{\partial r_{cx}} & \frac{\partial f_z}{\partial r_{cy}} & \frac{\partial f_z}{\partial r_{cz}} \end{bmatrix}_{r_c=r_{eq}}$$

These partial derivatives are provided in Appendix A. The procedure for finding the equilibrium point velocity \vec{r}_{eq} is provided in Appendix B. The simple harmonic oscillator equation is solved as a polynomial eigenvalue problem⁹, providing three eigenvalue pairs, each pair corresponding to harmonic motion in one eigenvector direction. The eigenvalues for each axis can be real, distinct pairs or complex conjugate pairs depending on the amount of damping in the system. The solution of the linearized equations along each eigenvector is then

$$\begin{aligned} \Delta r_c &= r_c - r_{eq} = Ae^{a_1 t} + Be^{a_2 t} \\ \Delta \dot{r}_c &= \dot{r}_c - \dot{r}_{eq} = Aa_1 e^{a_1 t} + Ba_2 e^{a_2 t} \end{aligned} \quad (2.7)$$

for cases where the eigenvalues are real and distinct values a_1 and a_2 . For cases where the eigenvalues are a complex conjugate pair $a \pm bi$, the solution is

$$\begin{aligned} \Delta r_c &= r_c - r_{eq} = Ae^{at} \cos bt + Be^{at} \sin bt \\ \Delta \dot{r}_c &= \dot{r}_c - \dot{r}_{eq} = Aae^{at} \cos bt - Abe^{at} \sin bt + Bae^{at} \sin bt + Bbe^{at} \cos bt \end{aligned} \quad (2.8)$$

The values of constants A and B can be determined with the initial conditions of $\Delta r_{c,t0}$ and $\Delta \dot{r}_{c,t0}$. These analytic equations can be solved to predict the motion of the confluence point, removing the need to integrate its equations of motion. This approach effectively locates the confluence point by averaging over the high frequency motion, motion which is generally along the longitudinal direction of the system. The axes of high frequency motion can be determined by examining the eigenvalue pairs found in the linearized characteristic equation in Eq. (2.6).

2.2 Validation

A simple model is used to study the analytic method, in which the attachment points are held at fixed locations while the confluence point is free to oscillate. The system is shown in Fig 2.1 below, with the corresponding physical parameters listed in Table 2.1. Note that the system is similar to a small mass suspended by two damped springs, where the triple bridles placed closely together can be represented by a single equivalent spring. This observation gives way to the prediction of high frequency motion in the z axis with lower frequencies in the lateral x and y axes, as the restoring forces in the lateral directions are very small relative to the vertical forces.

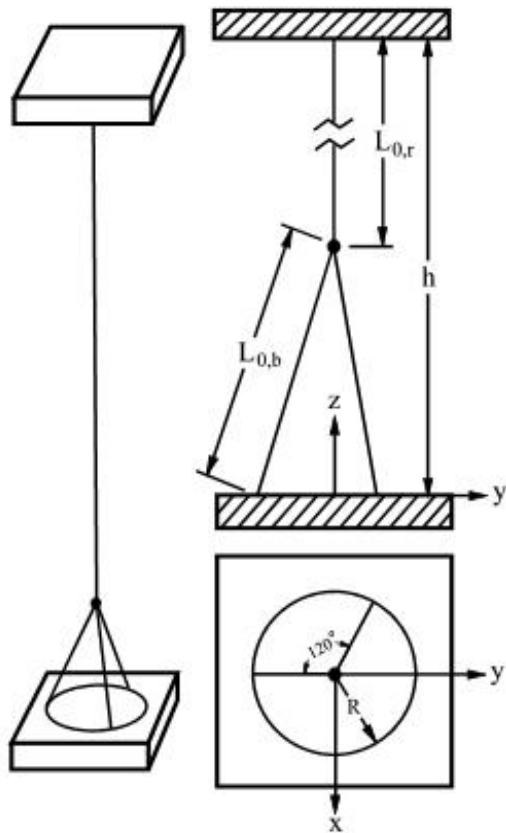


Table 2.1 Simple model specifications

Parameter	Value
C_b	100 N-s/m
C_r	300 N-s/m
h	36.2161 m
K_b	50,000 N/m
K_r	90,000 N/m
$L_{0,b}$	6 m
$L_{0,r}$	30 m
m_c	15 kg
R	1 m

Fig. 2.1 Simple confluence motion model

Given the value of h , the system is vertically stretched such that the uppermost attach point is 0.3 m above a system with all lines at free-stretch length. This input ensures the lines are taut throughout the simulation. The x and y components of the uppermost connection point are zero. The location of the equilibrium point can be found by resolving the forces on the confluence point geometrically, or by Newton-Raphson iteration for more complex configurations. The equilibrium point is

$$r_{eq} = \begin{bmatrix} 0 \\ 0 \\ 6.0305 \end{bmatrix} m$$

Equation (2.6) is evaluated independently of the initial confluence point position, providing

$$\bar{C} = \begin{bmatrix} 4.0142 & 0 & 0 \\ 0 & 4.0142 & 0 \\ 0 & 0 & 591.97 \end{bmatrix} \frac{Ns}{m} \quad \bar{K} = \begin{bmatrix} 5292.8 & 0 & 0 \\ 0 & 5292.8 & 0 \\ 0 & 0 & 236060 \end{bmatrix} \frac{N}{m}$$

The matching two values along the diagonal of the equivalent damping and stiffness matrices indicate symmetries in the system in the lateral directions x and y . This lateral symmetry, as well as the correlated terms being zero is a result of the system being axisymmetric along z in this equilibrium position. Evaluation of the polynomial eigenvalue problem⁹ for Eq. (2.6) provides

$$\lambda_x = \lambda_y = -0.1338 \pm 18.7839i$$

$$\lambda_z = -19.732 \pm 123.89i$$

The natural frequencies and damping ratios are derived, and are provided in Table 2.2.

Table 2.2 Linearized case equivalent parameters

Direction	$\omega_n, rad/s$	T, s	ξ
x	18.7843	0.3345	0.0071
y	18.7843	0.3345	0.0071
z	125.4485	0.0501	0.1573

Observation of the parameters in Table 2.2 indicates rapid oscillations of the confluence mass in the z axis. This high frequency motion was expected as the largest components of restoring tension lie

along the z axis. The system symmetry at equilibrium dictates lower, equivalent frequencies and damping ratios in the lateral x and y directions. The confluence mass motion over 5 seconds is predicted via the analytic solution as well as with integration of the equations of motion with an initial confluence point position and velocity defined in Table 2.3.

Table 2.3 Confluence initial conditions

Direction	r_0, m	$\Delta r_0, m$	$\dot{r}_0 = \Delta \dot{r}_0, m/s$
x	0.04	0.04	-1.0
y	0.05	0.05	1.0
z	6.06	0.0295	5.0

The analytic solution for position of the confluence mass with respect to the equilibrium point is shown in Fig. 2.2. The significant difference between frequencies and damping ratio in the lateral and longitudinal directions is clearly indicated. For a given configuration of the line connection points, the confluence quickly oscillates about a plane intersecting the equilibrium point while its projected position in that plane revolves the equilibrium point. Damping values then determine how fast the confluence point settles towards equilibrium. With regard to a computer simulation, this dictates that the confluence mass would never theoretically reach the equilibrium point within descent trajectory integration, let alone during a single time step.

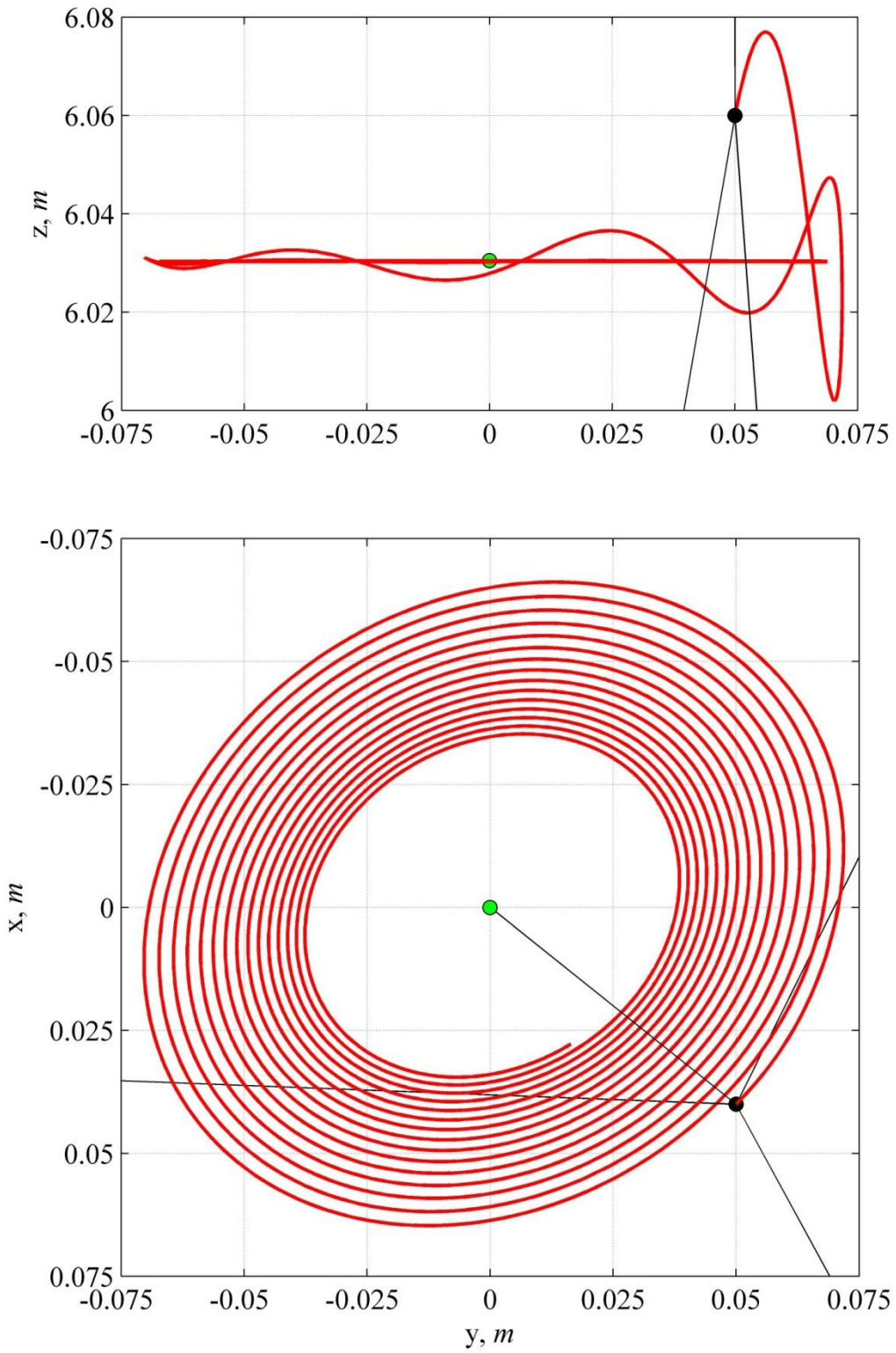


Fig. 2.2 Confluence analytic position with respect to equilibrium point

The analytic solution for position from evaluation of Eq. (2.8) is compared against the integrated solution in Fig. 2.3 over the first 0.5 seconds of motion. This integrated data is output from the variable time step integrator ode45 within Matlab[®], which utilizes 4th and 5th order Runge-Kutta integration. Processing times were 0.0654 s and 2.3804 s for the analytic and integrated solutions, respectively. The analysis was performed on an Intel Centrino[®] Duo machine equipped with Windows Vista[™]. Position is measured with respect to the equilibrium point, which is constant and equivalent between output methods. Note that forces due to gravity are ignored in both data sets. The analytic position and velocity of the confluence mass approximately match the integrated solution for this simple case. Differences in position are seen in the lateral directions x and y, where the analytic solution oscillates at slightly different amplitude than the integrated position. High frequency motion in the longitudinal z axis is matched to within 0.3 mm at the largest deviation. The calculated values of natural frequency and damping ratio in Table 2.2 from the linearized characteristic equation are also in agreement with the oscillations seen in the integrated position.

Large deviations in output from the integrated position are observable when confluence point motion extends further from the equilibrium point, where linearization assumptions are no longer valid. Cases where the confluence point is initially located outside this region or when the confluence initial velocity propels it there can cause significant errors in output from the analytic solution. Non-linearity in the equations of motion becomes increasingly influential in asymmetric bridle tension conditions, limiting this region of validity further. Such asymmetry can be observed in this simple system by laterally deflecting the uppermost connection point, resulting in an equilibrium point off the z-axis.

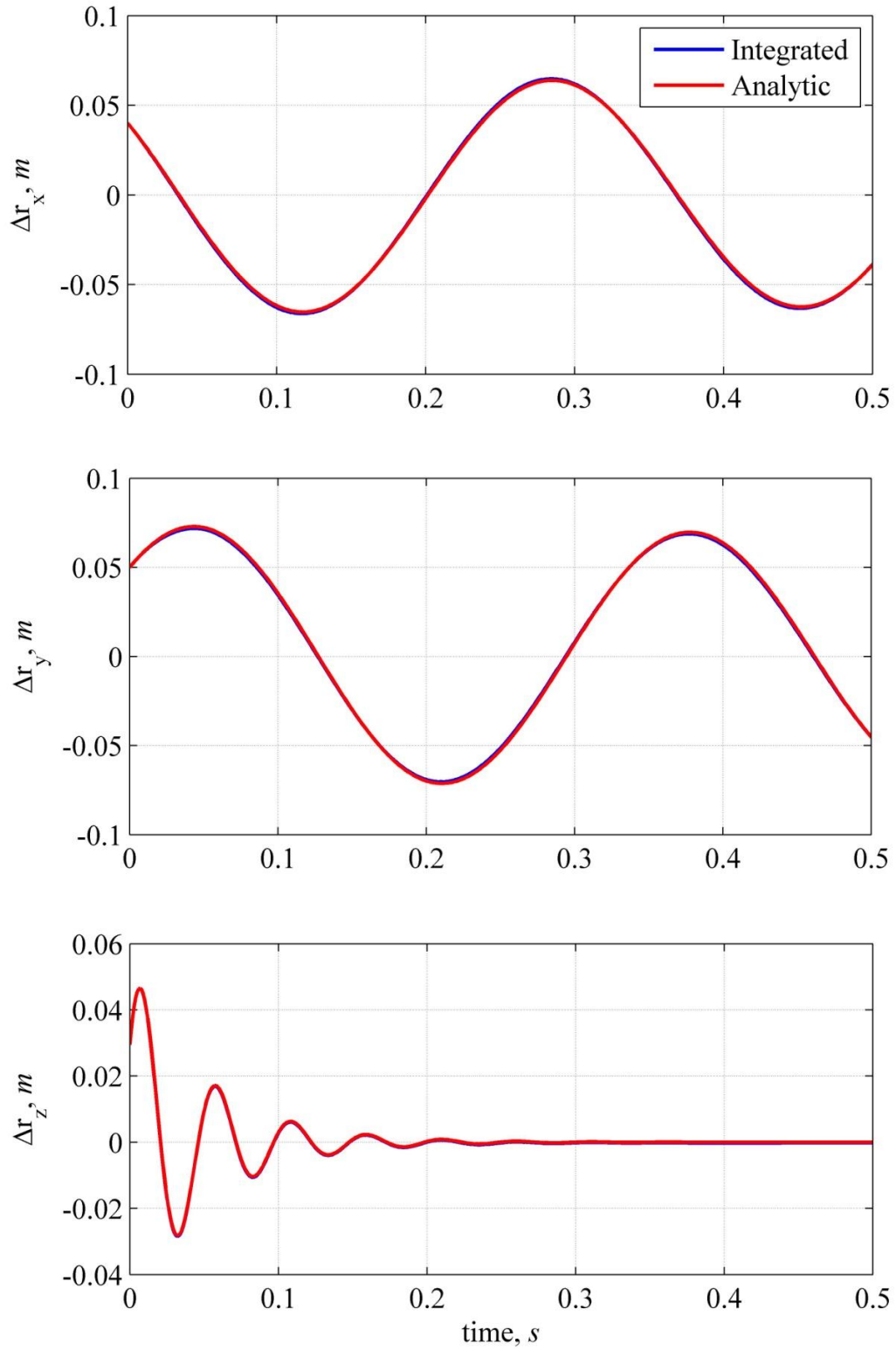


Fig. 2.3 Analytic and integrated comparison of confluence position

2.3 Discussion

The analytic solution method presented here constitutes a procedure to predict confluence point motion with respect to the equilibrium point. Past approaches⁷ involving the equilibrium point solution provided a solution of simply placing the confluence point at the equilibrium point within each time step. This method ignores the confluence point motion resulting from its position and velocity while displaced from equilibrium. The analytic method can be used to identify axes of high frequency motion and used to average this high frequency over a larger time step than full integration requires. Theoretically, using the analytic method to predict confluence position and velocity within a single integration time step should then produce results of greater similarity to the fully integrated result. There are several points of discussion that explore the effectiveness of the analytic method:

1. Calculation of the equilibrium point in a high-fidelity parachute descent simulation is a significant obstacle, given high instances of slack connecting lines and frequent non-convergence of iterative solvers.
2. The analytic method presented requires significantly more computations than the equilibrium method, given that the linearization coefficient matrices and characteristic eigenvalues must be calculated in addition to the equilibrium point within each time step.
3. As the equilibrium method already places the confluence point at the long period averaged position about which the analytic method oscillates, it is likely the analytic method offers insignificant improvements to data accuracy.

The primary difficulty in implementing this method within a high-fidelity entry, descent, and landing simulation is the calculation of the equilibrium point within each integration time step. Calculation of the equilibrium point is performed by way of a Newton iterative solver in which the confluence position which satisfies

$$\sum_{i=1}^N \vec{T}_i = \sum_{i=1}^N K_i (\|\vec{r}_i - \vec{r}_c\| - L_{0,i}) \hat{n}_i = 0 \quad (2.9)$$

The solver can be remarkably effective in well-conditioned cases in which all lines are taut where an accurate initial guess is provided. Conversely, the solver is prone to non-convergence in cases which lines may be slack. Given the condition that no lines provide compressive forces, the solver will also diverge if a single iteration propagates the equilibrium solution to a point where any line is slack. In the event of a slack line, the solver provides an equilibrium position resolved by the attachment points of the remaining taut lines. The subsequent iteration results in an extreme corrective tension from the previously slack line coupled with possible slackness in the previously taut lines. Consequently, a single slack instance within the Newton iterative solver produces considerable instability resulting in non-convergence. Both the equilibrium point solution and the analytic solution derived from it here are subject to these problems of non-convergence.

It was determined while implementing the equilibrium point solution that for Runge-Kutta 4th order integrators, the equilibrium point must be evaluated within each intermediate slope calculation of integration. This constitutes four iterative solutions per time step. The analytic solution presented here requires an additional calculation of the equilibrium point velocity, the linearized equivalent stiffness and damping matrices in Eq. (2.6), and the eigenvalues. The method would thus require significantly more processing time than the equilibrium method alone.

It is observed that the motion of the more massive rigid bodies of the system is generally unaffected by small deviations in position and velocity of the less massive confluence point.

Consequently, output data from the equilibrium point solution, a method which effectively eliminates high frequency oscillation of the confluence point, shows satisfactory agreement to a fully integrated solution that requires a significantly lower time step. It is then questionable that using the analytic method presented would drastically improve results by predicting the high frequency motion previously ignored.

Given the reasoning presented above, implementation of the analytic method within a complex parachute trajectory simulation was avoided. Difficulties in defining acceptable initial conditions in which no slack events are encountered as well as in maintaining confluence point position within the region of linear assumption validity prohibited further investigation of this method. Future work in the matter would require a more robust solution procedure for determining the equilibrium point. It would also behoove the analyst to prove the analytic method provides superior accuracy over the equilibrium point solution, and that the improvement is worth the additional computational requirements required.

3 Singular Perturbation Method

3.1 Theory

The singular perturbation method, like the equilibrium point solution, aims to replace the numerically stiff equations of motion for the confluence mass with other less computationally expensive means. Examination of Eq. (1.2) indicates the source of the stiffness is the very large acceleration value resulting from tension values being divided by the small confluence mass. This equates to a problem of singular perturbation, where some small parameter on the highest order derivative in a system of equations may not be approximated by setting the parameter to zero. Here, the mass of the confluence may not be set to zero without causing singularity.

Consider the limiting case as the confluence point mass approaches zero where the number of lines attached to the mass is generalized. As the mass approaches zero, so must the limit of the left hand side of in Eq. (1.2):

$$\lim_{m_c \rightarrow 0} (m_c \ddot{\vec{r}}_c) = \sum_{i=1}^N \vec{T}_i = 0 \quad (3.1)$$

The limit provides an equilibrium relation at the confluence point with N attached lines. The equilibrium point solution⁷ uses this equation to solve for the equilibrium point location, eliminating the equations of motion of the confluence point from the system. On the other hand, the singular perturbation solution uses this equation to determine the velocity $\dot{\vec{r}}_c$ which is integrated along with the other equations of motion to provide the inertial position. Solving for the velocity of the confluence point requires expanding the tension equation.

Each tension vector is defined by

$$\vec{T}_i = [K_i(\|\vec{r}_i - \vec{r}_c\| - L_{0,i}) + C_i(\vec{r}_i - \vec{r}_c) \cdot \hat{n}_i] \hat{n}_i \quad (3.2)$$

where

$$\hat{n}_i = \frac{(\vec{r}_i - \vec{r}_c)}{\|\vec{r}_i - \vec{r}_c\|} \quad (3.3)$$

and \vec{r}_i is the inertial position of the attachment point of line “i” to the vehicle or parachute. Recall that compressive forces will be ignored since many parachute trajectory models only allow tensile forces. Expanding Eq. (3.2) and rearranging provides

$$\sum_{i=1}^N C_i(\vec{r}_c \cdot \hat{n}_i) \hat{n}_i = \sum_{i=1}^N [K_i(\|\vec{r}_i - \vec{r}_c\| - L_{0,i}) + C_i \vec{r}_i \cdot \hat{n}_i] \hat{n}_i \quad (3.4)$$

Solving for \vec{r}_c obtains

$$\vec{r}_c = \alpha^{-1} \left\{ \sum_{i=1}^N [K_i(\|\vec{r}_i - \vec{r}_c\| - L_{0,i}) + C_i \vec{r}_i \cdot \hat{n}_i] \hat{n}_i \right\} \quad (3.5)$$

where

$$\alpha = \sum_{i=1}^N \begin{bmatrix} C_i n_{ix}^2 & C_i n_{ix} n_{iy} & C_i n_{ix} n_{iz} \\ C_i n_{ix} n_{iy} & C_i n_{iy}^2 & C_i n_{iy} n_{iz} \\ C_i n_{ix} n_{iz} & C_i n_{iy} n_{iz} & C_i n_{iz}^2 \end{bmatrix} \quad (3.6)$$

Note that α is the linearized equivalent damping matrix \bar{C} , as damping force is linear in the confluence point velocity. The solution obtained is a continuous function until the system reaches a situation where any of the attached lines go slack, such that this slack line provided the only opposing tension to the remaining taut lines. In the presence of a slack line, the matrix α becomes non-invertible resulting in a singularity in Eq. (3.5). This condition is caused when there is no confluence velocity that will maintain the equilibrium amongst the remaining lines in tension.

Line slackness was a considerable obstacle to the analytic solution presented as well as the equilibrium method referenced, and has often been a troublesome issue among multibody trajectory

simulations. One method generally used to circumvent the problem is the inclusion of a confluence damping force. Past models have often used excessive confluence damping forces to reduce the high frequency motion that this method seeks to alleviate. Unfortunately, introducing the damping force contaminates the motion of the system when compared to the results from applying a mass at the confluence point, when no damping force is necessary for slack cases.

In this study, a minimal confluence damping force is applied only in the amount necessary to propagate the integration through instances of singularity. The confluence damping, without which equilibrium would be impossible, is required to balance the net force from the remaining lines in tension. The confluence damping force is defined by

$$\vec{F}_d = -C_c(\vec{r}_c - \vec{r}_{c,0}) \quad (3.7)$$

where $\vec{r}_{c,0}$ is the inertial velocity of the confluence point from the previous integrated time step. This previous velocity must be included because the damping force is reliant upon the relative velocity of the confluence point with respect to the system, not the inertial velocity. Subtracting this term serves to eliminate the inertial component of the confluence velocity. The damping force is added to Eq. (3.1), providing

$$\left(\sum_{i=1}^N \vec{T}_i \right) + \vec{F}_d = 0 \quad (3.8)$$

Substituting Eqs. (3.2) and (3.7) into Eq. (3.8) and rearranging obtains

$$\left(\sum_{i=1}^N C_i(\vec{r}_c \cdot \hat{n}_i) \hat{n}_i \right) + C_c \vec{r}_c = \left(\sum_{i=1}^N [K_i(\|\vec{r}_i - \vec{r}_c\| - L_{0,i}) + C_i \vec{r}_i \cdot \hat{n}_i] \hat{n}_i \right) + C_c \vec{r}_{c,0} \quad (3.9)$$

Solving for the confluence velocity provides the damped confluence solution

$$\vec{r}_c = [\alpha]^{-1} \left\{ \left(\sum_{i=1}^N [K_i(\|\vec{r}_i - \vec{r}_c\| - L_{0,i}) + C_i \vec{r}_i \cdot \hat{n}_i] \hat{n}_i \right) + C_c \vec{r}_{c,0} \right\} \quad (3.10)$$

where

$$[\alpha] = \left(\sum_{i=1}^N \begin{bmatrix} C_i n_{ix}^2 & C_i n_{ix} n_{iy} & C_i n_{ix} n_{iz} \\ C_i n_{ix} n_{iy} & C_i n_{iy}^2 & C_i n_{iy} n_{iz} \\ C_i n_{ix} n_{iz} & C_i n_{iy} n_{iz} & C_i n_{iz}^2 \end{bmatrix} \right) + C_c \begin{bmatrix} 1 & 0 & 0 \\ 0 & 1 & 0 \\ 0 & 0 & 1 \end{bmatrix} \quad (3.11)$$

Note that when there are no slack lines, confluence damping is not used or $C_c = 0$.

The method was evaluated where the user input a constant confluence damping coefficient. This was undesirable because the physical definition of confluence damping is vague at best and setting a value is equivalent to guessing. Additionally it was found that there was always some lowest value of damping that resolved slack cases and introduced the least contamination into the system for that particular set of initial conditions and system parameters. Damping below that particular value C_c does not result in a well-conditioned α matrix, resulting in a termination of the simulation. Unfortunately it may be difficult for a first-time user to determine this acceptable value, since cases that include mass at the confluence point may not be available for comparison with the singular perturbation method. These problems associated with a constant damping value necessitated the development of a method to determine C_c without requiring user input.

Determining an acceptable value of confluence damping at each slack case that arises requires a way to rank the matrix α according to how “close” it is to singularity. Understanding that the matrix is singular and therefore non-invertible when damping is not included, it is also found that any value of C_c added to the diagonal elements will make the matrix non-singular. Therefore using singularity as a metric for grading acceptable matrices α is not sufficient. Small amounts of damping, while making the matrix non-singular, will still allow some analyses to become unstable. Determining if a matrix is nearly singular can be accomplished using a condition number commonly used in linear algebra. The condition number is defined by

$$\kappa = \|\alpha\| \|\alpha^{-1}\| \quad (3.12)$$

Matrix α is ill-conditioned if a small relative change in α causes a large relative change in its inverse¹⁰. The degree of ill-conditioning is gauged by the condition number κ . Using the Frobenius norm of the symmetric matrix α , the condition number reduces to

$$\kappa = \sqrt{\text{trace}(\alpha^2) \cdot \text{trace}((\alpha^{-1})^2)} \quad (3.13)$$

Increasing the diagonal values of matrix α drives the condition number lower. Low condition numbers indicate a matrix is well-conditioned, providing a metric to use in the incremental application of damping to slack cases. The value of the required condition number is ultimately up to the analyst, but for these proceedings a value of 5 was used and found acceptable.

Implementing the singular perturbation method within most integrators is relatively unobtrusive. When the state vector is evaluated for the equations of motion, the integration of acceleration of the confluence point is disregarded and the velocity is obtained via Eq. (3.10). Slack line cases require adding increments of C_c within each particular time step until the appropriate conditioning is obtained. The velocity of the confluence point is then integrated to determine the position of the confluence point. This method eliminates the integration of acceleration from the analysis, increasing the minimum required time step. Effectively the singular perturbation method replaces the three velocity state equations without the need for iterative solvers within each time step.

3.2 Validation

Validation of the singular perturbation method requires comparison to models that have mass at the confluence point, models that use this mass to evaluate the full set of equations of motion. The simulation software used to test the method is the Program to Optimize Simulated Trajectories II (POST2)⁸. The original POST software package was developed by Lockheed Martin for NASA and was used to optimize ascent and reentry trajectories of the Space Shuttle. The program has been modified and upgraded extensively over the past decades for use with all types of re-entry problems encountered by planetary landers. Of particular relevance is the enhanced capabilities to model multibody vehicular configurations, allowing POST2 to simulate mixed 3 and 6 degree-of-freedom attached bodies within the same analysis⁵. The established and verified multibody capability using a point mass for the confluence point allows POST2 to simulate parachutes. The attaching lines are modeled by massless spring-dampers as presented in the theory section. The following subsections present results comparing POST2 results for MER test cases and the CEV abort mode, using both the unmodified equation of motion solution and the singular perturbation method.

3.2.1 Mars Exploration Rover Simulation

The Mars Exploration Rover (MER) entry configuration was chosen to model initial cases using the singular perturbation method. This particular configuration has been modeled in past studies⁵⁻⁶ to validate multibody simulations, providing some legacy with which to compare the results from this study. The entry model, like many Mars lander simulation models, consists of the rigid body vehicle attached via three bridles to a swivel confluence point, which is connected to the rigid body parachute with a single riser. The configuration with dimensions is shown below in Fig. 3.1. The system properties used for this section are detailed in Tables 3.1 and 3.2.

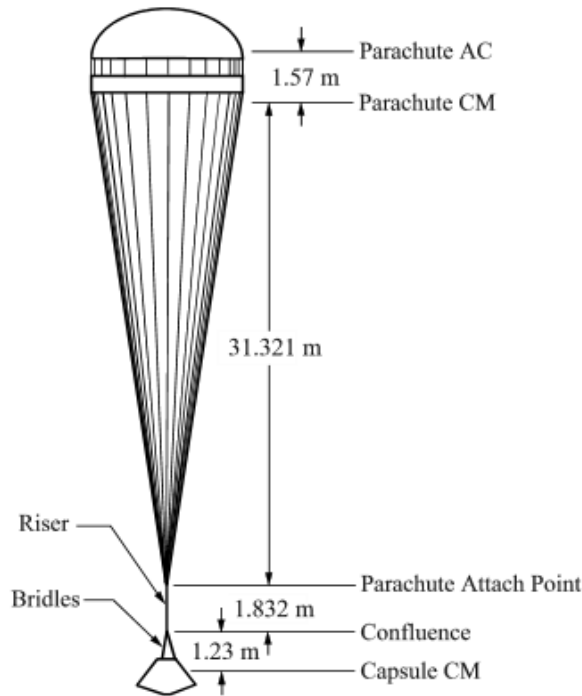


Table 3.1 MER model line properties

Line	L_0, m	$K, N/m$	$C, N-s/m$
Bridles	0.7152	47,000	470
Riser	1.832	60,000	600

Table 3.2 MER model mass properties

	Vehicle	Confluence	Parachute
DoF	6	3	6
m, kg	761.0	0.1539	16.00
I_{xx}, kgm^2	238.02	N/A	253.7
I_{yy}, kgm^2	179.13	N/A	1126.5
I_{zz}, kgm^2	212.51	N/A	1126.5

Fig. 3.1 MER descent configuration

The body axes used for the vehicle as well as the attachment point and center of mass locations are shown in Fig. 3.2. The bridle attachment points are placed 120° apart. All test cases except cases 5 and 6 begin with the x body axis pointed to nadir, the y body axis pointed East, and the z body axis pointed South. The simulation used a non-rotating, elliptical Mars planet model with spherical gravity. All MER simulations start at zero latitude and longitude at an approximate altitude of 8.4 km. The planet model parameters are detailed in Table 3.3. To simulate the Martian environment, an atmospheric model was used to vary density with altitude. The density profile is shown in Fig. 3.3. The atmospheric density was used to calculate the aerodynamic forces of the parachute only. The aerodynamic forces on the vehicle and confluence point are neglected in all test cases.

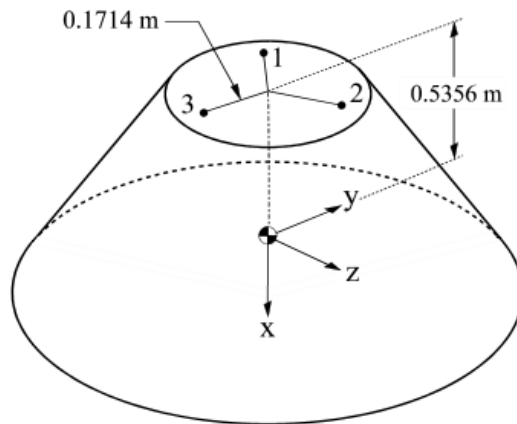


Fig. 3.2 MER body axes and bridle attachment points

Table 3.3 Mars planet model parameters

Parameter	Value
μ	$4.282828685 \times 10^{13} \text{ m}^3/\text{s}^2$
R_e	$3.393940 \times 10^6 \text{ m}$
R_p	$3.376780 \times 10^6 \text{ m}$
$J_2, J_3, J_4 \dots$	0.0
Ω	0.0 rad/s

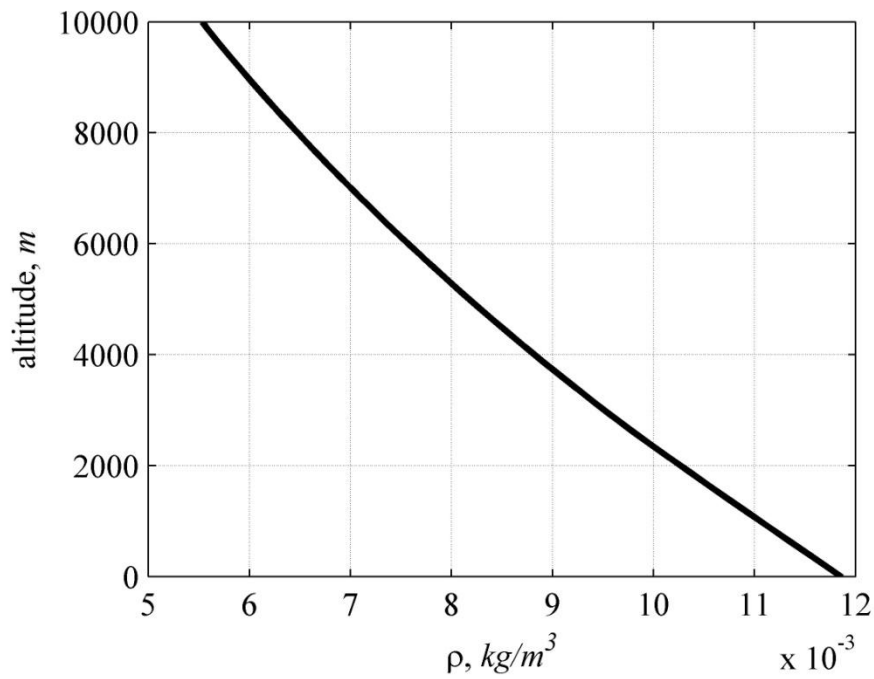


Fig. 3.3 Mars atmospheric density profile

The parachute and shroud lines in the simulation are modeled as a single rigid body with aerodynamic data as a function of the parachute angle of attack. A constant drag value of 0.46 was used for the axial force coefficient. The values of C_N used are shown in Fig.3.4. The forces are applied at the parachute aerodynamic center, located 1.57 meters above the parachute center of mass. The parachute has a reference area of 178.47 m² and it begins with an initial orientation with the x body axis pointed to nadir, the y body axis pointed East, and the z body axis pointed South for all test cases.

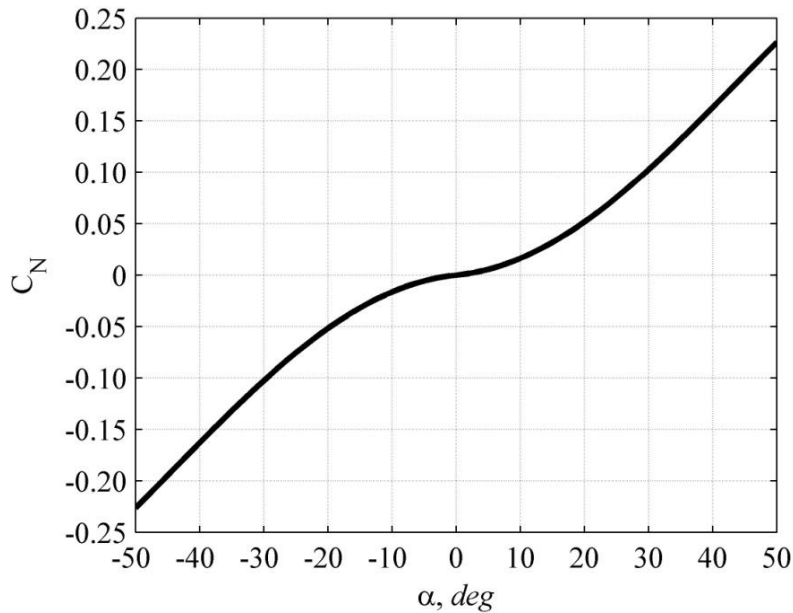


Fig. 3.4 MER zero trim parachute model

The system model was subjected to several test cases that sought to exploit particular dynamic motion. The initial conditions of each case were varied to individually examine the desired dynamics such as swinging or excessive line slackness. Test case 1 begins with the configuration dropped from rest, and positioned so that all lines are at stretch-free length. Test case 2 is identical to test case 1, except the parachute is positioned 1 cm lower in altitude to introduce initial slackness in the connecting lines. Test cases 3 and 4 are identical to case 1, except the vehicle is given an initial lateral velocity to the East and South, respectively, causing frequent and asymmetric slackness in the three bridles. Test cases 5 and 6 begin with the initial configuration with the lines at free-stretch length with the vehicle rotated 10 degrees about the z and y axes, respectively. The vehicle begins with an initial downward velocity in test cases 5 and 6 as well. For cases 1 through 4, the full mass solution uses an integration time step of 0.0001 seconds and the singular perturbation solution uses a time step of 0.01 seconds. Cases 5 and 6 used a singular perturbation time step of 0.002 s.

Test case 1 for the MER configuration serves to validate the singular perturbation method in the most simplified of cases. This case also establishes a baseline model for the gravitational and aerodynamic effects for subsequent tests. The fully deployed configuration shown in Fig. 3.1 is dropped from rest. The line tensions start at zero and increase to the maximum loading at terminal velocity. The initial conditions are detailed in Table 3.4. The bridle tension history is shown in Fig 3.5. The difference in line loading between the triple bridles is negligible compared to the high tensions experienced during the simulation. The singular perturbation method results show agreement to the full equation of motion solution in all line loadings to within 1 Newton and 6 Newtons for the bridles and riser, respectively.

Table 3.4 MER test case 1 initial conditions

Body	Altitude, m	North Velocity, m/s^2	East Velocity, m/s^2	Down Velocity, m/s^2
Vehicle	8380.217	0.0	0.0	0.0
Confluence	8381.447	0.0	0.0	0.0
Parachute	8414.600	0.0	0.0	0.0

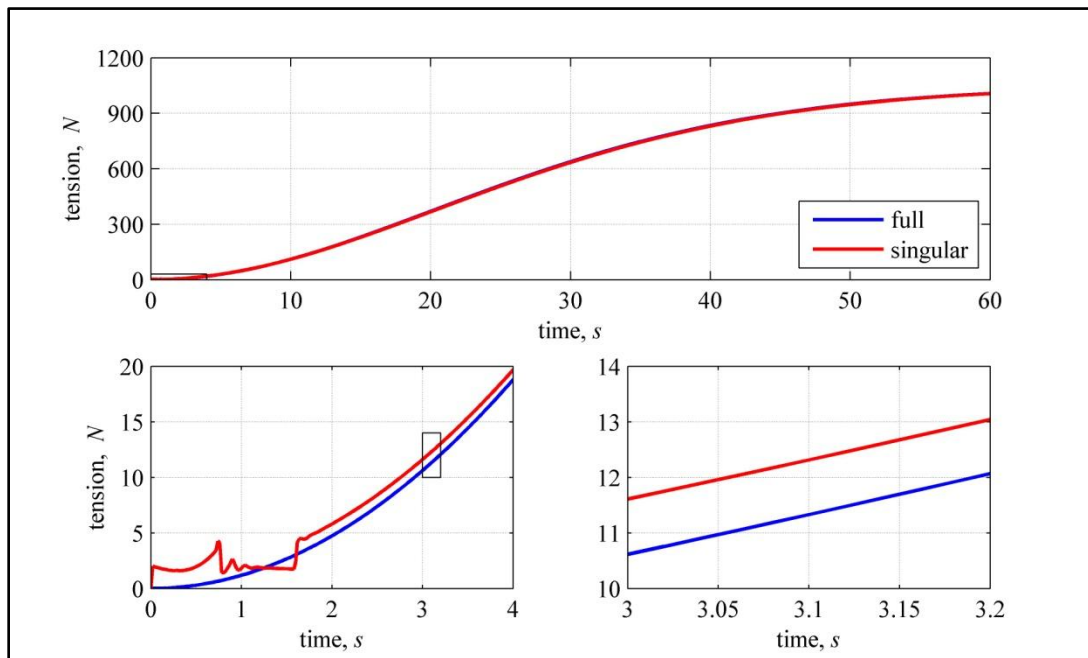


Fig. 3.5 Test case 1 tension history of bridles

The initial 2 seconds of the simulation are of particular interest because of the erratic force profile of the singular perturbation method. This behavior is attributed to the initial slackness of all lines which institutes the use of confluence point damping. The damping force is activated if any of the lines are slack, and the riser is noticeably slack for the first second. Once the solution has propagated past the slack instances, the confluence damping force is removed and the force profile settles to the same trend as the fully integrated solution. The small, relatively constant difference in the force profiles is attributed to the initial imposed confluence damping force. The orientation and lateral inertial position of all 3 bodies remain unchanged for the entire duration, and the final capsule altitudes for the full and singular solutions are 4258.2 m and 4268.0 m, respectively.

Test case 2 begins with the parachute located 1 cm closer to the confluence point, resulting in slackness in the main riser. Table 3.5 gives the initial conditions of the case. Since aerodynamic forces are only applied to the parachute, the capsule and confluence point initially fall faster than the parachute. The resulting effect is a rapid excitation of the confluence point due to the sudden tensile forces exerted when the riser becomes taut. The results from the full solution and singular perturbation solution for test case 2 are shown in Fig. 3.6 and Fig. 3.7.

Table 3.5 MER test case 2 initial conditions

Body	Altitude, m	North Velocity, m/s^2	East Velocity, m/s^2	Down Velocity, m/s^2
Vehicle	8380.217	0.0	0.0	0.0
Confluence	8381.447	0.0	0.0	0.0
Parachute	8414.590	0.0	0.0	0.0

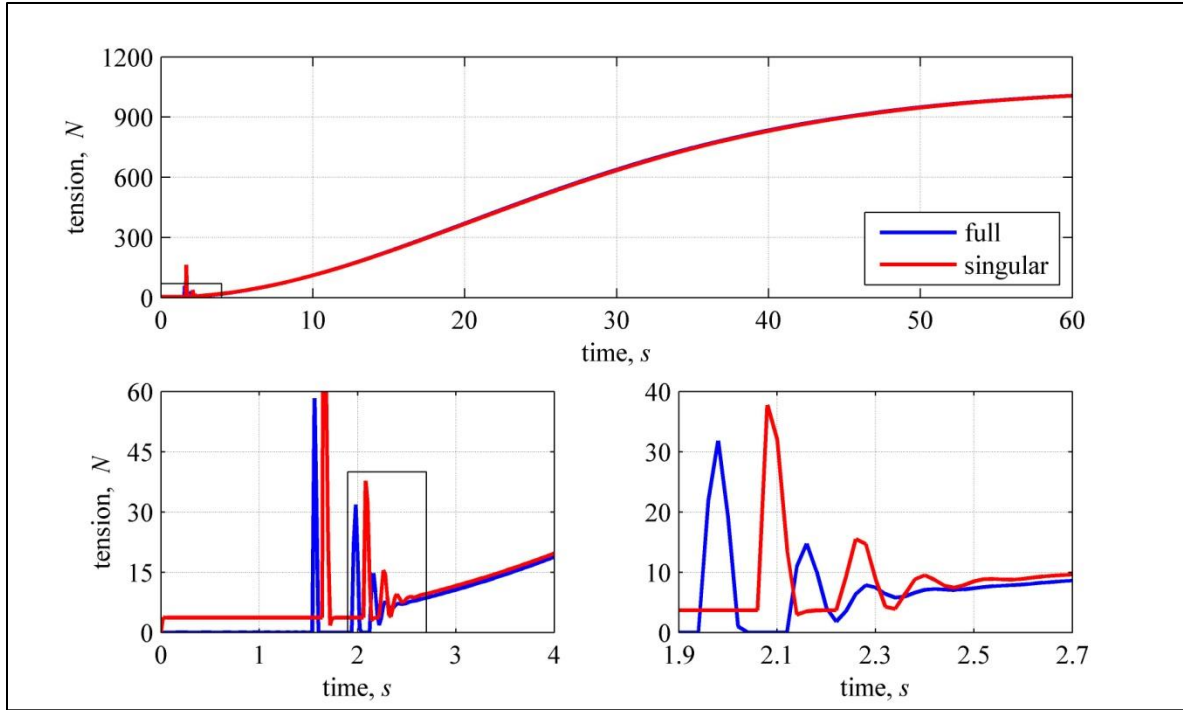


Fig. 3.6 Test case 2 tension history of bridles

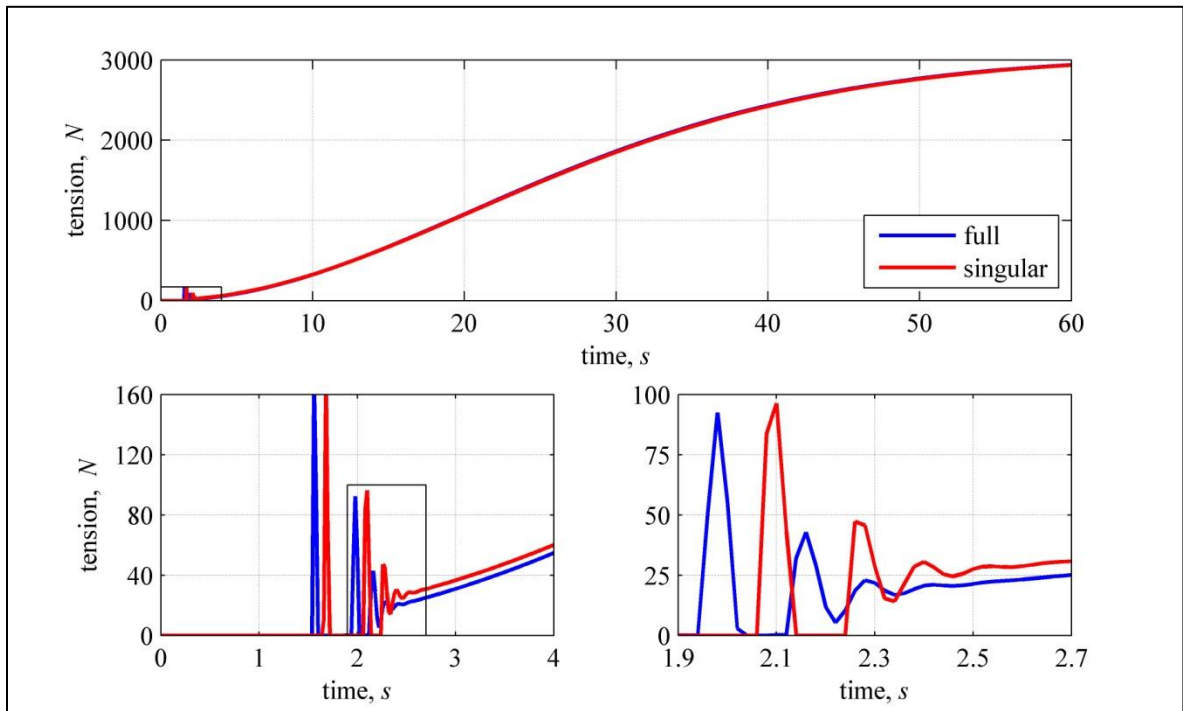


Fig. 3.7 Test case 2 tension history of riser

As in test case 1, the difference in line loading between the triple bridles is negligible. Several slack instances follow the excitation, highlighting the confluence damping effects that must be applied with the singular perturbation method. The initial 3 seconds of the tension profiles show similar behavior between the triple bridle and riser force profiles. Both methods capture the sudden excitation of the confluence point, with a slight phase lag between the full solution and the singular solution profiles. The amplitude and period of the tensions are separated by a lag of approximately 0.1 seconds. The lag seen in the singular perturbation solution is a result of the confluence point falling relatively slower than in the fully integrated case. This is caused by the confluence point damping force appearing in place of the slack parachute riser. The damping force is opposed by the small tensions of approximately 4 Newtons seen each of the three bridles in the singular perturbation data. The excitation then settles to the steady increase seen in test case 1, now separated by no more than approximately 10 Newtons between the two data sets. The orientation and lateral inertial position of all 3 bodies remain unchanged for the entire duration, and the final capsule altitudes for the full and singular solutions are 4258.2 m and 4268.1 m, respectively.

Test case 3 is designed to evaluate the results of the singular perturbation method in the event of frequent slackness in the connecting lines. This effect is achieved by imparting an initial lateral velocity on the capsule while leaving the parachute and confluence point unchanged. Table 3.6 details the initial conditions of test case 3. The vehicle is given a

Table 3.6 MER test case 3 initial conditions

Body	Altitude, m	North Velocity, m/s^2	East Velocity, m/s^2	Down Velocity, m/s^2
Vehicle	8380.217	0.0	1.0	0.0
Confluence	8381.447	0.0	0.0	0.0
Parachute	8414.600	0.0	0.0	0.0

lateral velocity in the East direction, which will cause bridle 3 to be initially slack. The results are shown in Figs. 3.8 through 3.11. Bridles 1 and 2 are initially taut, exciting the confluence point and causing slack instances in all four connecting lines early in the simulation. Note that the movement of the bodies remains in the XY body plane of the capsule, so tensions in triple bridles 1 and 2 are identical.

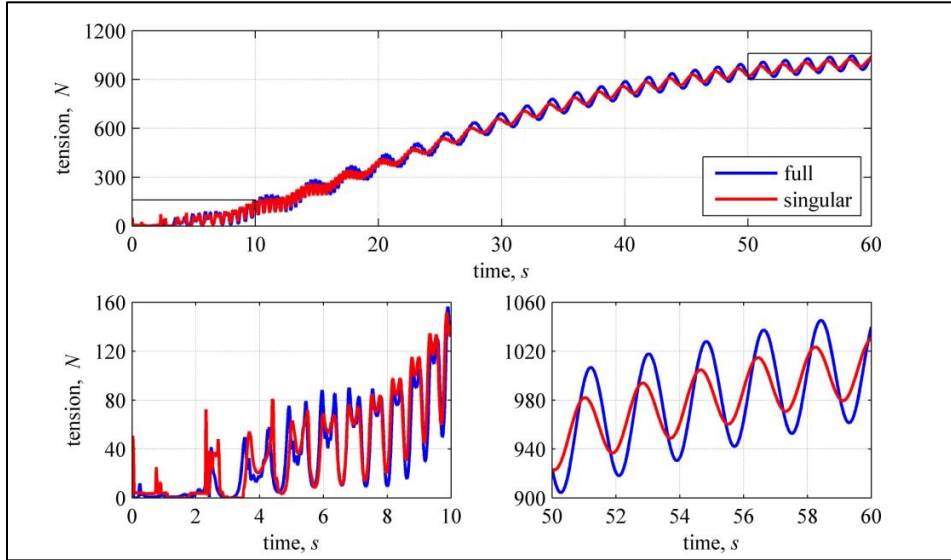


Fig. 3.8 Test case 3 tension history of bridle 1

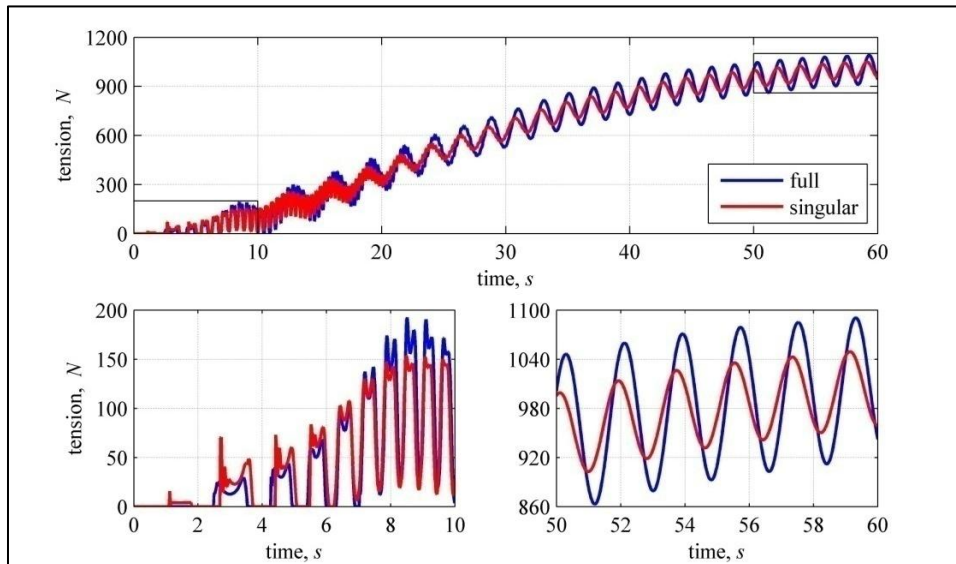


Fig. 3.9 Test case 3 tension history of bridle 3

The first 10 seconds of the tension profiles confirm multiple slack instances amongst all connecting lines. The resulting difference in the singular perturbation method as compared to the full solution has the same phase lag seen in test case 2. As the high frequency motion of the confluence point settles, the long period frequency caused by capsule swing dominates the remainder of the simulation. The long period frequency in the triple bridle profiles is essentially the same between the data, though again separated by a slight phase lag attributed to earlier use of confluence damping. The amplitude of the full solution profile in this region is approximately twice that of the singular perturbation solution. The tension of the parachute riser in this time span has fully settled in both data sets, separated by a difference of approximately 6 Newtons.

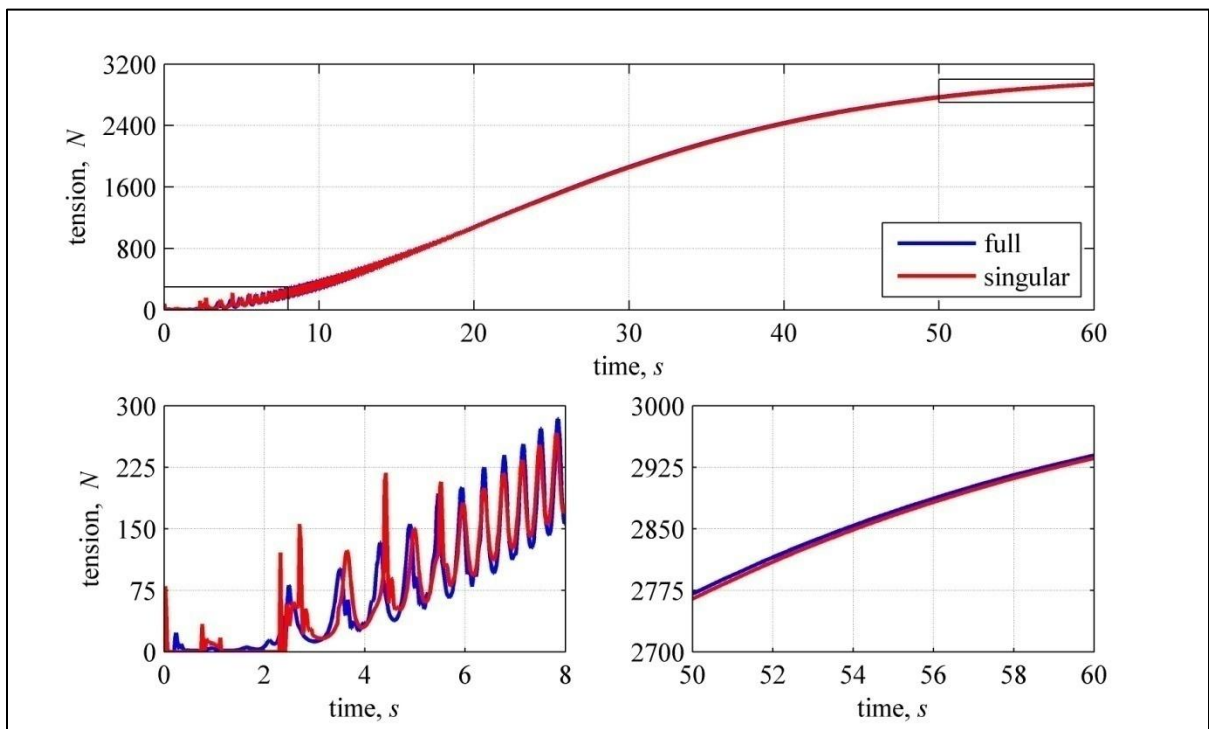


Fig. 3.10 Test case 3 tension history of riser

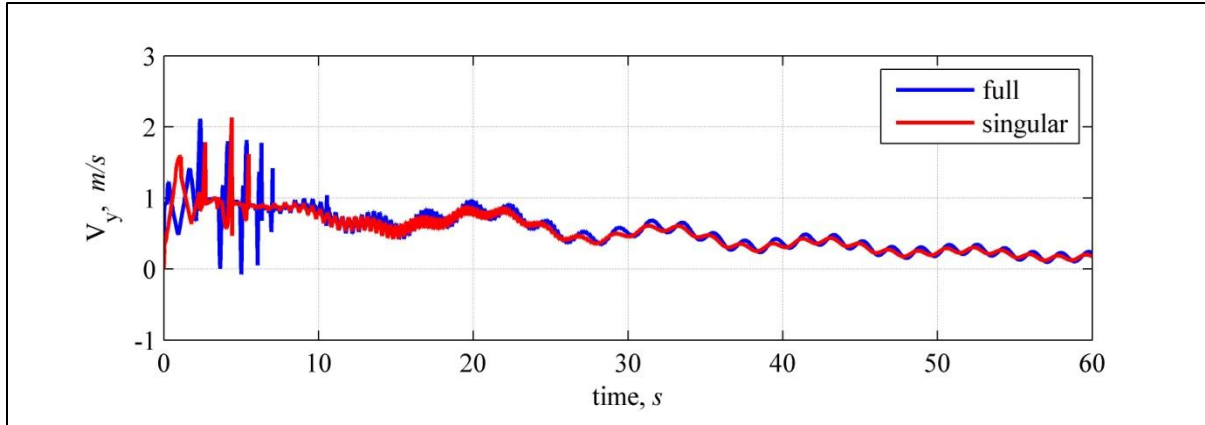


Fig. 3.11 Test case 3 confluence point lateral velocity

The initial high frequency oscillation of the tension profiles attributed to the rapid oscillation of the confluence point, shown by the lateral inertial velocity profile in Fig. 3.11. This velocity profile is closely matching in shape and frequency between the two methods. The long period oscillation shows that the average value of velocity is closer matched than the high frequency oscillations, as is also demonstrated in the line tension profiles. The final inertial lateral position of the capsule differs by 1.2 meters, and the final altitude of the capsule differs by 9.0 meters between data sets.

Test case 4 is another case designed to examine the results in cases with frequent occurrences of slackness, however with the motion confined to be coplanar to the XZ capsule body plane. This motion is interesting because it represents the most asymmetric line loading possible. The initial conditions for test case 4 are shown in Table 3.7. The test case begins much like test case 3, except the lateral velocity on the capsule is applied in the Northern direction. The asymmetric effects are traced to bridles 1 and 2, which rapidly “trade” instances of slackness early in the simulation. The results for test case 4 are shown in Figs. 3.12 through 3.15.

Table 3.7 MER test case 4 initial conditions

Body	Altitude, m	North Velocity, m/s^2	East Velocity, m/s^2	Down Velocity, m/s^2
Vehicle	8380.217	1.0	0.0	0.0
Confluence	8381.447	0.0	0.0	0.0
Parachute	8414.600	0.0	0.0	0.0

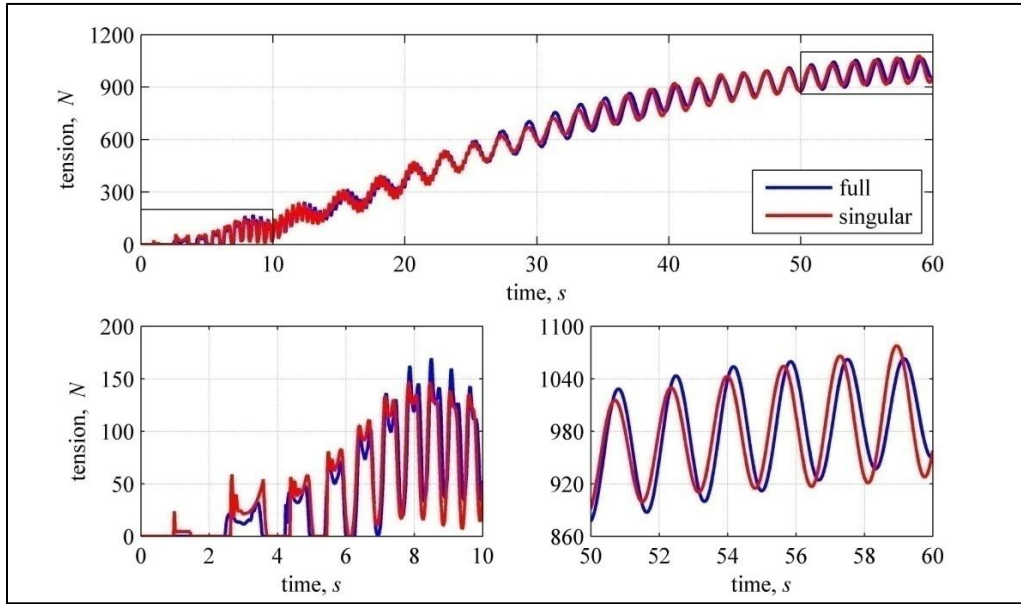


Fig. 3.12 Test case 4 tension history of bridle 1

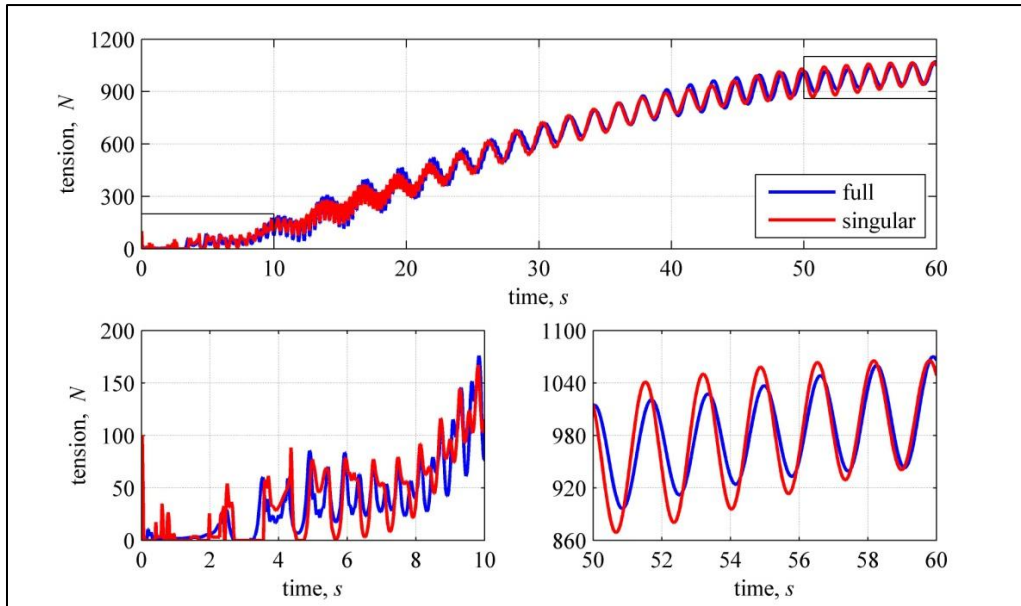


Fig. 3.13 Test case 4 tension history of bridle 2

The initial tension profiles for bridles 1 and 2 verify instances of slackness induced for alternating periods. The singular perturbation solution approximately matches the full solution in all connecting lines over the first 10 seconds with less short period, high frequency behavior. As the confluence point high frequency motion settles and leaves intact the long period tension oscillations from capsule swing, bridles 1 and 2 have alternating periods where the full solution and singular solution match in phase and amplitude. The long period oscillations for bridle 3 are nearly identical in period and amplitude between data sets, yet separated by a phase lag of approximately half of the wavelength. The phase lag has little impact on the orientation and position of the capsule or parachute, but rather on the confluence point. As mentioned earlier, the overall time-dependent position of the confluence point is of little importance to the trajectory analyst, provided there is negligible change in the dynamics of the more massive bodies.

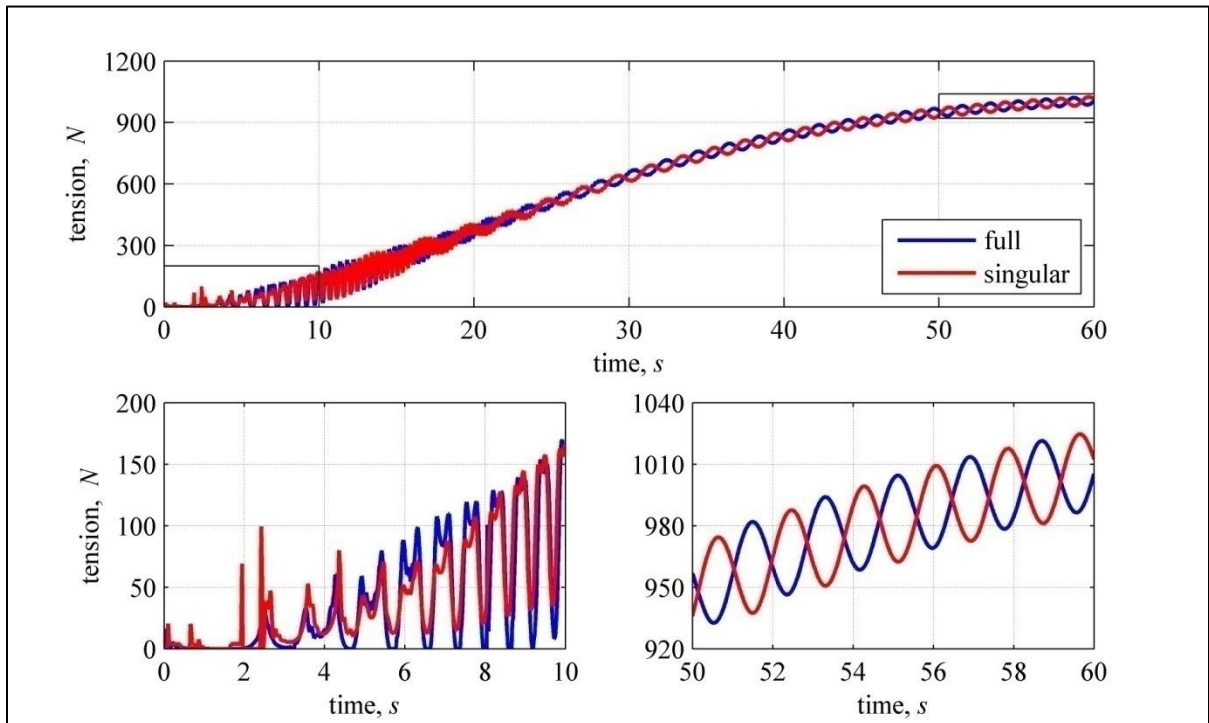


Fig. 3.14 Test case 4 tension history of bridle 3

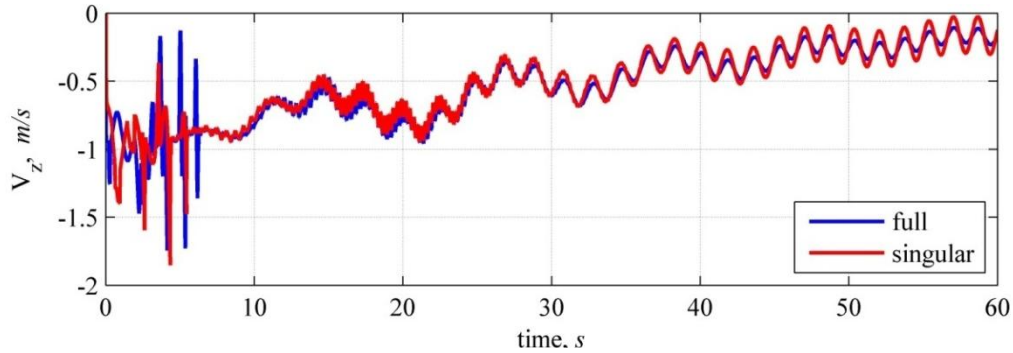


Fig. 3.15 Test case 4 confluence point lateral velocity

The confluence lateral velocity in Fig. 3.15 shows remarkable similarity between output sets. Initial disagreements due to frequent line slackness are quickly resolved in the first 6 seconds, followed by general agreement in both short and long period motion. Agreement between the averaged values of lateral velocity across the entire simulation assures accuracy in the confluence integrated position, resulting in agreement in the overall system dynamics for both outputs. The final inertial lateral position of the capsule differs by 0.95 meters between data sets, and the final altitude of the capsule differs by 9.3 meters.

Test case 5 begins with the capsule rotated 10 degrees about the +Z body axis and positioned such that the confluence point is located in the same location as previous tests with the triple bridles at their free-stretch lengths. All vehicles begin with a downward velocity of 10 m/s initiating higher initial parachute drag, as starting the simulation from rest has been thoroughly studied. The initial conditions of test case 5 are detailed in Table 3.8. The initial rotation of the capsule serves to induce swinging, or another method to rapidly excite the confluence point. Line slackness is also observed, however less severe in occurrence when compared to test cases 3 and 4. The results for test case 5 are shown in Figs. 3.16 through 3.19. Note that the motion of the system is confined coplanar to the XY capsule body plane, resulting in identical tension profiles in bridles 1 and 2.

Table 3.8 MER test case 5 and 6 initial conditions

Body	Altitude, m	North Velocity, m/s^2	East Velocity, m/s^2	Down Velocity, m/s^2
Vehicle	8380.236	0.0	0.0	10.0
Confluence	8381.447	0.0	0.0	10.0
Parachute	8414.600	0.0	0.0	10.0

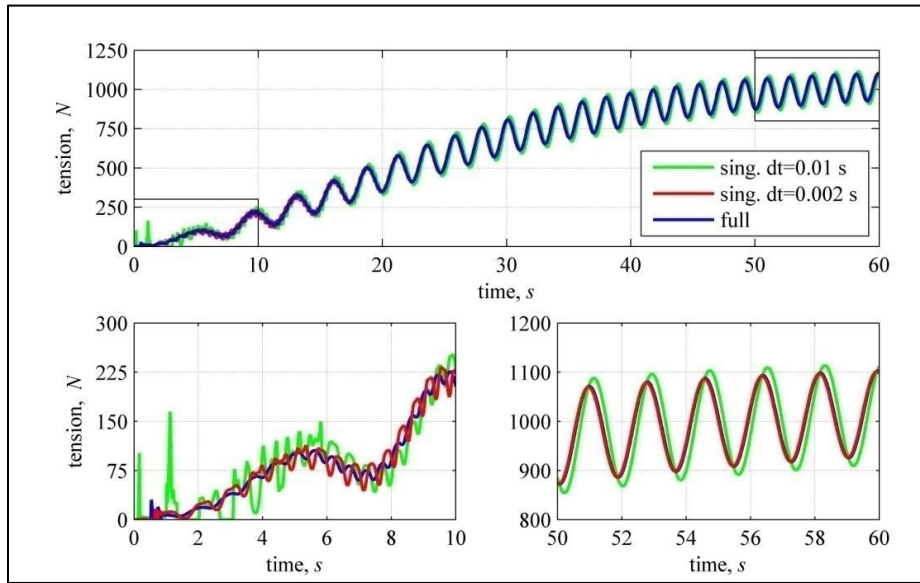


Fig. 3.16 Test case 5 tension history of bridles 1 and 2

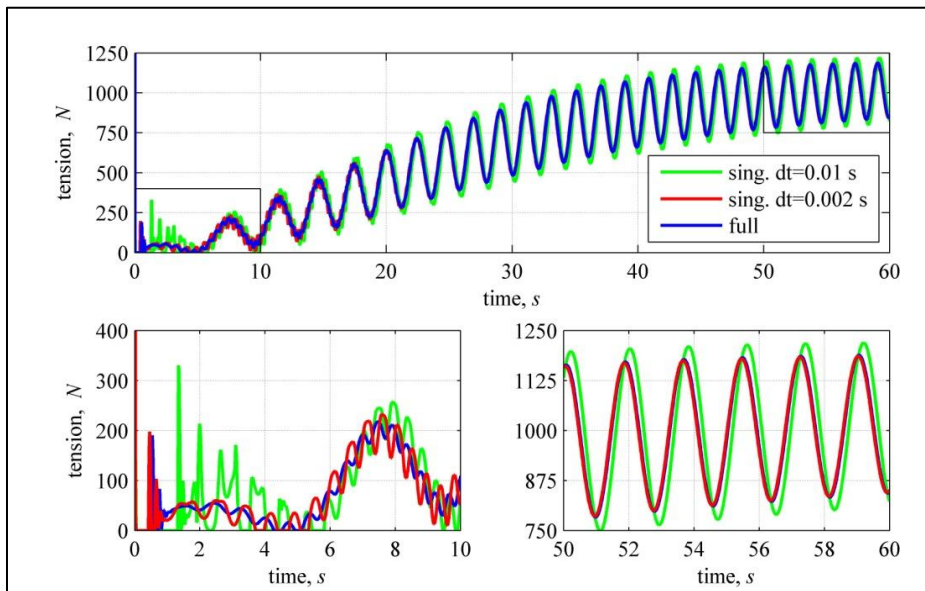


Fig. 3.17 Test case 5 tension history of bridle 3

The early portions of the simulation show stark differences between the two methods, with the singular perturbation solution giving more high frequency behavior than the full solution. It was determined that lower time steps reduced this artifact, as shown by the singular output when run at a time step of 0.002 seconds. It is evident that with the singular perturbation method, care must be taken in choosing integration time steps for cases in which there is more high frequency motion of the confluence point. The method still affords higher time steps than full integration, however. Fortunately, the averaged tension values agree despite the differences seen here. Later in the simulation, when the confluence point motion has settled, the oscillations in bridle tension show agreement between methods in both frequency and amplitude. Note that the case in which the time step was 0.01 seconds showed agreement in average tension values following confluence settling, despite the high frequency artifacts introduced early on.

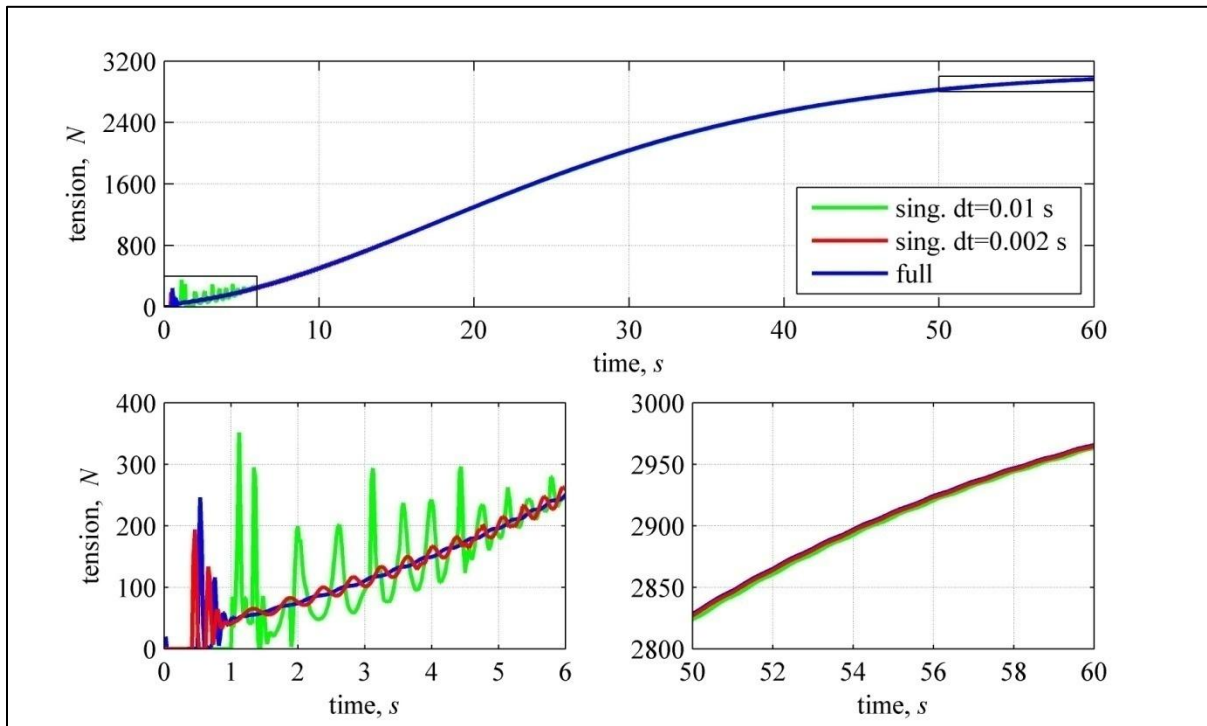


Fig. 3.18 Test case 5 tension history of riser

The singular output riser tension in Fig. 3.18 shows the effects of the high frequency artifacts as well, with a much longer settling period of the confluence than the integrated solution. The higher time step of 0.01 seconds indicates large oscillations introduced early in the profile. By the end of the simulation the riser tension profiles differ by no more than 4 Newtons between the full integration and the lower time step singular perturbation solution.

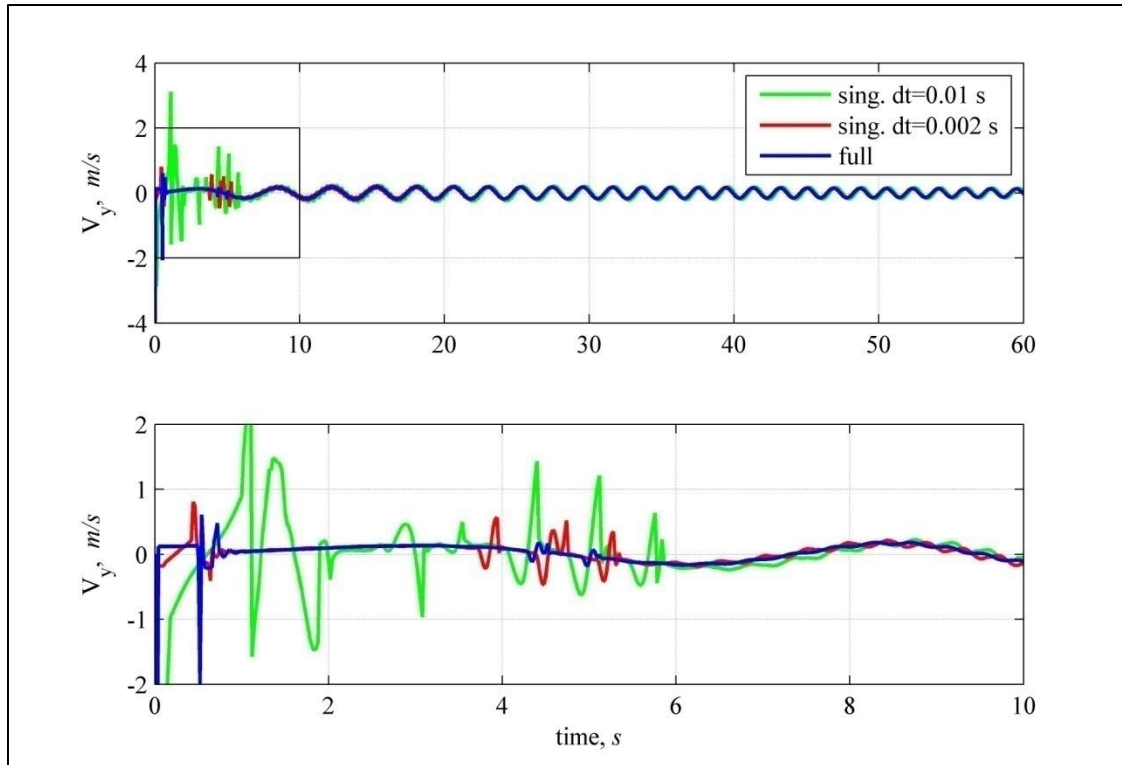


Fig. 3.19 Test case 5 confluence point lateral velocity

The confluence point lateral inertial velocity is plotted above, showing more high frequency effects in the singular perturbation output data. Initial deviations in the higher time step are evident here as they were in the tension profiles. The larger effect of line slackness on the confluence velocity from the singular solution is evident following the 4 second mark as well. The later portion after confluence point settling shows agreement between averaged confluence velocities, and therefore confluence position output. Agreement between confluence behavior data prescribes

agreement in the dynamics of the capsule and parachute bodies. The final inertial lateral position of the capsule differs by 0.02 meters between the full integration and low time step singular data sets, and the final altitude differs by 2.0 meters. For the higher time step singular perturbation output, the final lateral position and altitude differ by 0.65 meters and 8.5 meters, respectively.

Test case 6 begins with the capsule rotated 10 degrees about the +Y body axis and positioned such that the confluence point is located in the same location as previous tests with the triple bridles at their free-stretch lengths. All bodies in the case also begin with a 10 m/s downward velocity. Similar to test case 5, this case seeks to examine the singular perturbation method results for extended swinging motion by the capsule. Unlike test case 5, this case will examine the motion coplanar to the XZ body plane. This motion causes asymmetric line loading in the bridles much like the scenario in test case 4. The initial conditions for test case 6 also in Table 3.8, with the exception of the vehicle rotated about the +Y body axis instead of the +Z body axis. The results from the full equation of motion solution and the singular perturbation method are shown in Figs. 3.20 through 3.24. The same high frequency artifacts seen in test case 5 were seen here with higher time steps, so a time step of 0.002 seconds was used for the singular perturbation method.

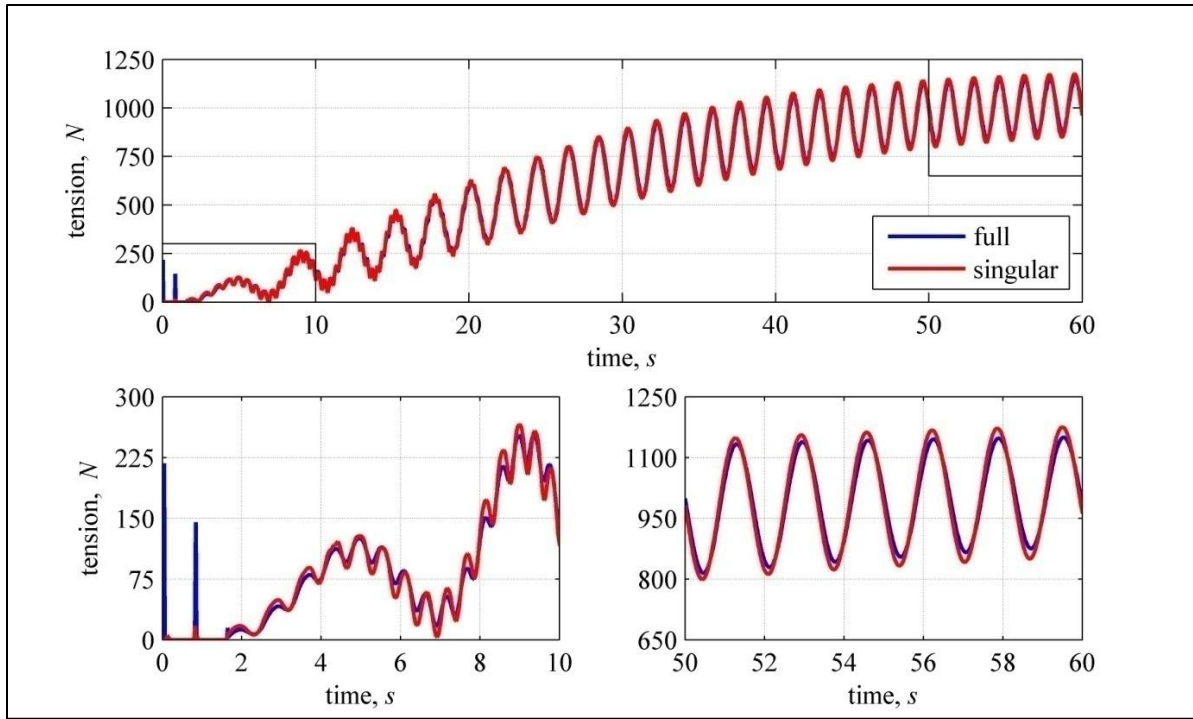


Fig. 3.20 Test case 6 tension history of bridle 1

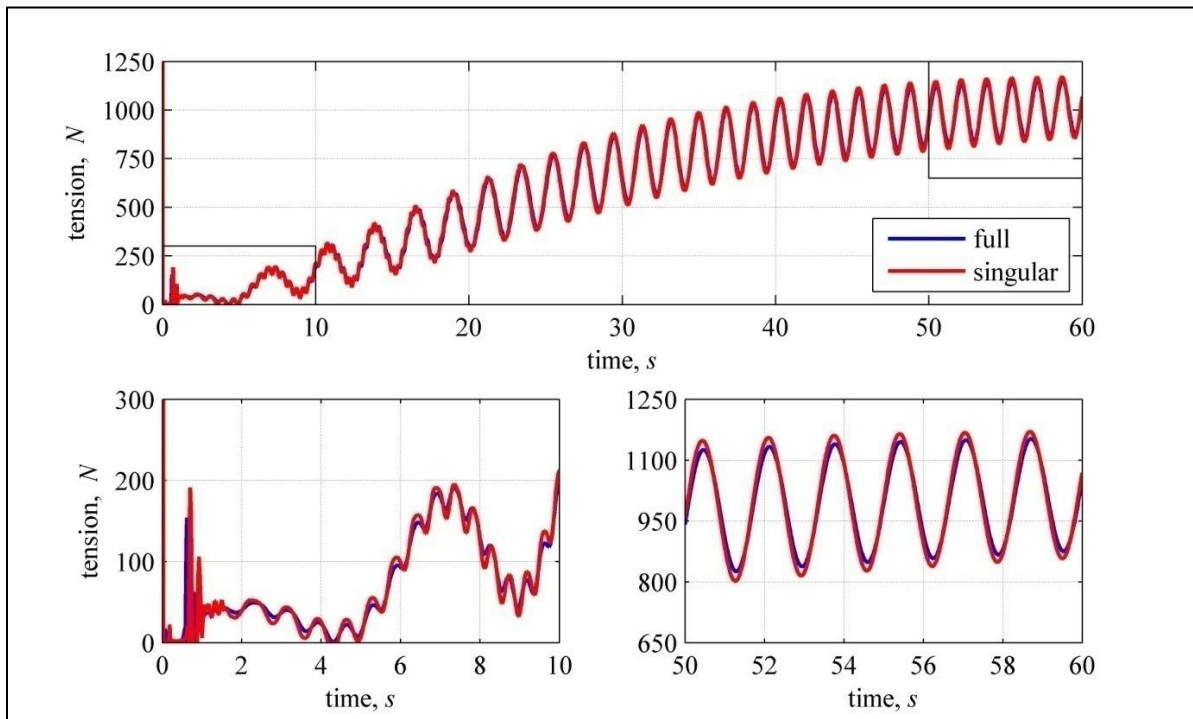


Fig. 3.21 Test case 6 tension history of bridle 2

The tensions in all lines show excessive high frequency motion in the initial 10 seconds of the singular perturbation method. Much like in test case 5, this motion is confirmed by the high frequency changes in the confluence point lateral inertial velocity in Fig. 3.23. After settling of the confluence point, the velocity output data agree in long period averaged value. The later, long period oscillations in bridle tension also show agreement in frequency and phase, with 10% larger amplitude from the singular output data for bridles 1 and 2. Bridle 3 shows agreement here in amplitude and frequency and amplitude, though showing a phase lag of half the wavelength. The riser tension profile shows negligible difference and is not pictured. The positioning of the capsule shows agreement between data sets, with a difference of 1.9 meters in final altitude and 0.026 m in lateral inertial position. The deviation in lateral position is most evident in the initial portion of the simulation where slack cases are being handled.

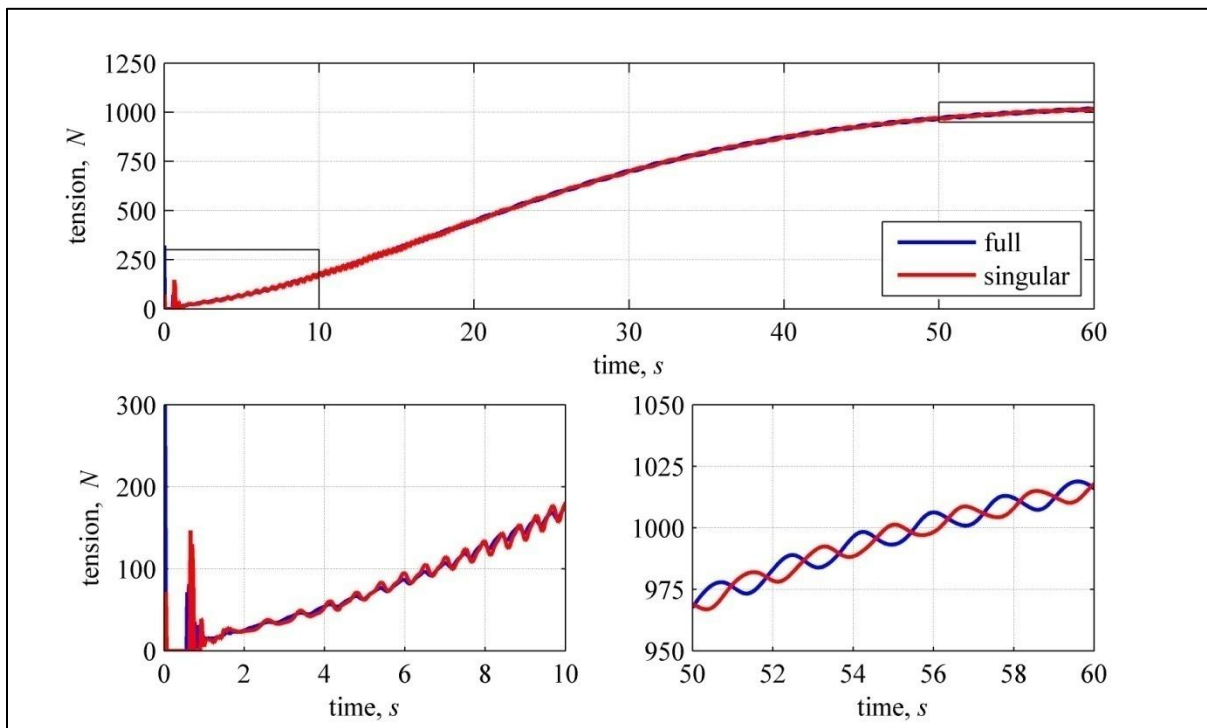


Fig. 3.22 Test case 6 tension history of bridle 3

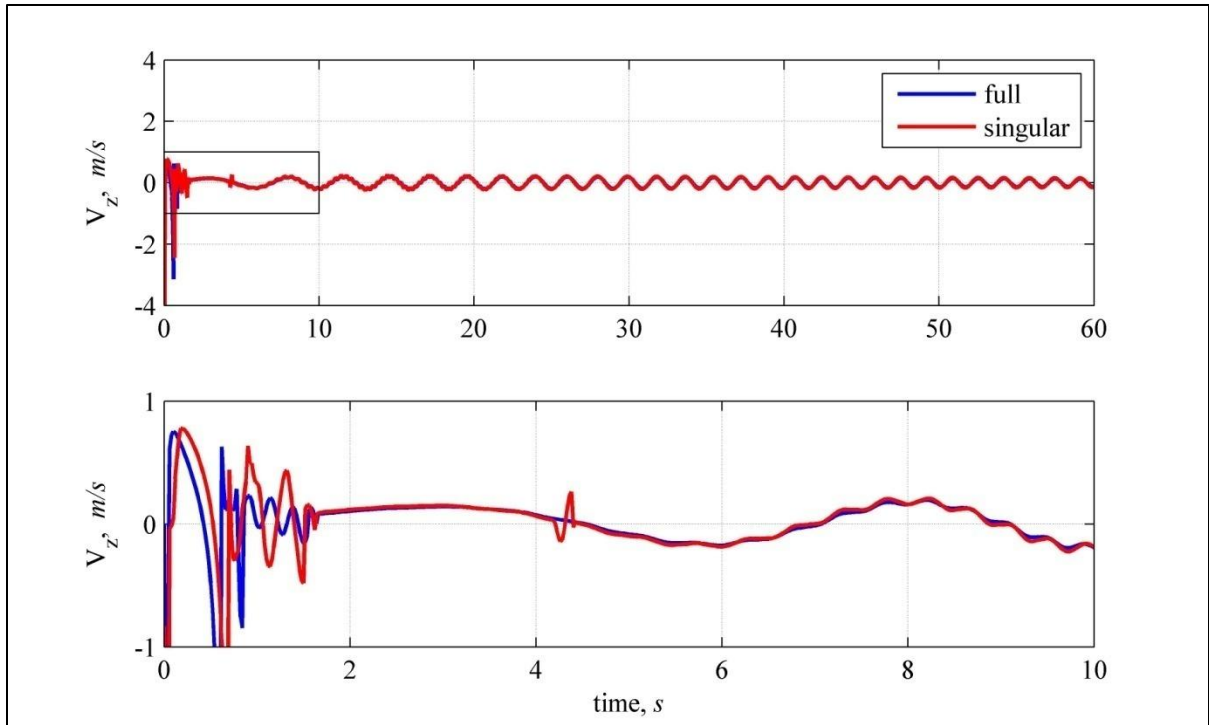


Fig. 3.23 Test case 6 confluence point lateral velocity

3.2.2 Crew Exploration Vehicle Simulation

The Crew Exploration Vehicle (CEV) is the next-generation vehicle being designed for manned space exploration. Similar in design to the Apollo tower abort systems, the CEV is scheduled for operation in 2014 and is currently in the design and test phases. The CEV will be capable of abort during early portions of the launch trajectory, enabled by an active-control abort tower situated at the apex of the capsule. The abort motor can be fired during launch to separate the CEV and propel it a safe distance from the launch vehicle. The tower then reorients the capsule to fly heat shield forward, and is then jettisoned along with the forward bay cover. The parachute systems are deployed to bring it safely back to the surface. The first integrated test for the abort system is called Pad Abort 1 (PA1) and is scheduled at the White Sands Missile Range in 2009. The PA1 test scenario occurs as described above with the exception that the abort motor is fired while the CEV is at rest on the launch pad.

Extensive research modeling the trajectory of the CEV abort mode, including that of PA1, has been conducted in the NASA Langley Atmospheric Flight Engineering Systems Branch. POST2 models involving six degree-of-freedom motion of the system have been used for the analysis. The system is comparable to the MER test case system employing a confluence point that deploys at line stretch, approximately 12 seconds after tower jettison. The similar models allow the singular perturbation method to be easily applied and evaluated in a complex analysis. The trajectory scenario in Fig. 3.24 marks the main events of the PA1 test case and the timing of the events in the actual test and singular perturbation simulation are shown in Table 3.9. Note that the simulation is not started until the tower jettison since the confluence point and main parachutes are not deployed until shortly afterward. As with the MER test bed, all simulations are conducted using both the full equation of motion solution with a mass applied at the confluence point and the singular perturbation method.

The parachute is modeled as a single rigid body as with the MER test cases. Aerodynamic forces are calculated for both the capsule and parachute rigid bodies. The full equation of motion solution requires a time step of 0.0005 s and the singular perturbation solution requires a time step of 0.01 s following parachute deployment. The simulation was run on a Red Hat® Linux AS4 machine with a single 2.8 GHz Intel Pentium processor. The full and singular analyses each took 80.57 s and 35.80 s of processing time, respectively. The results from the simulation are shown in Figs. 3.25-3.29.

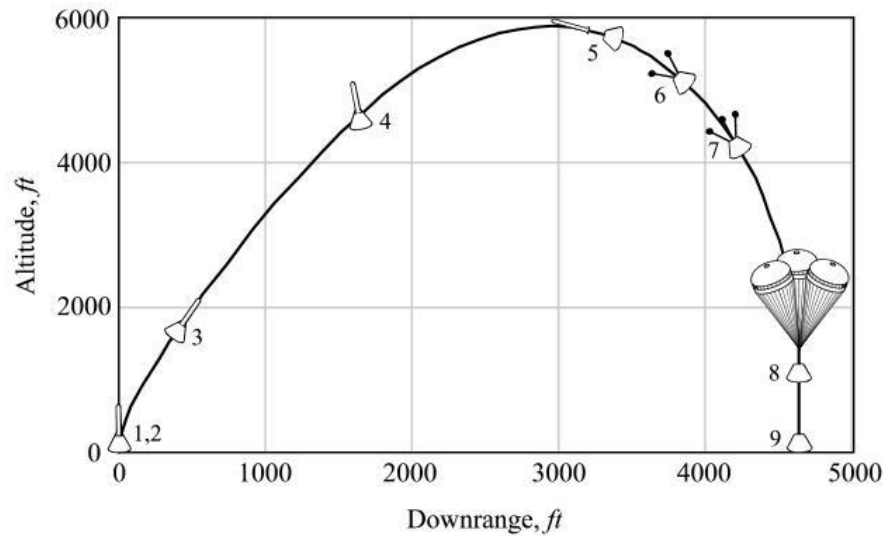


Fig. 3.24 CEV Pad Abort 1 test scenario

Table 3.9 Pad Abort 1 event log

Event ID	Description	Time since ignition, s	Simulation time, s
1	Ignition of abort and pitch motors	0.00	N/A
2	Liftoff	0.02	N/A
3	Abort motor tail off	2.60	N/A
4	Begin reorientation	10.00	N/A
5	Jettison tower	21.00	0.00
6	Deploy drogue parachutes	24.50	3.50
7	Deploy main parachutes	30.50	9.50
8	Attain 30 ft/s descent rate	52.74	31.74
9	Touchdown	99.87	78.87

Broad comparison shows good agreement between results from the full equation solution and singular perturbation solution. The tension histories of the connecting lines indicate portions of rapid load inductions as well as portions of settling that varies depending on the line number, providing ample variety of motion of the confluence point. All three bridles experience slack instances, briefly on bridle 1 and then significantly more frequent on bridles 2 and 3. The riser experiences a single slack instance for approximately 0.5 seconds just after the snatch loads from the parachute opening.

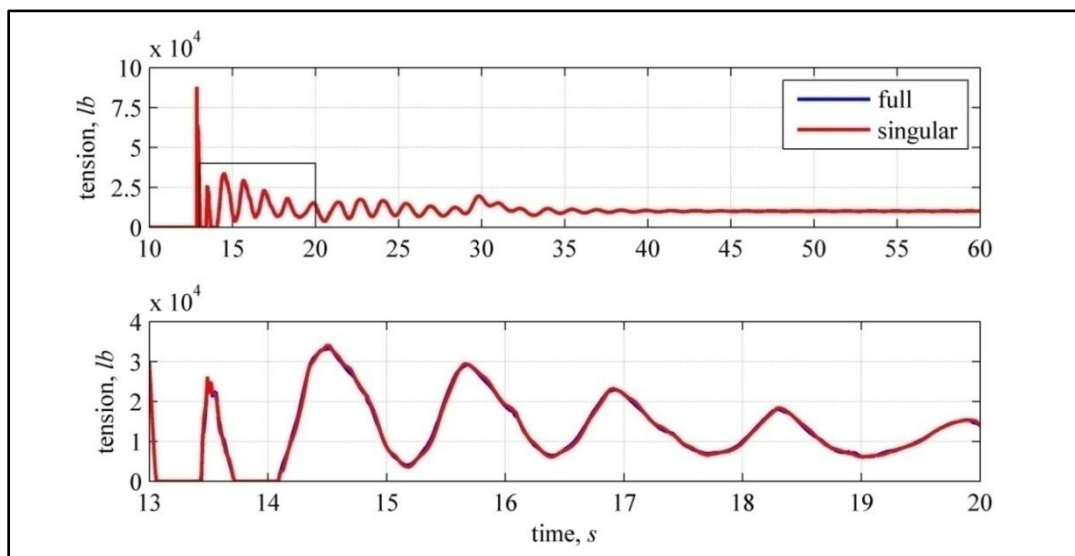


Fig. 3.25 Pad Abort 1 tension history of bridle 1

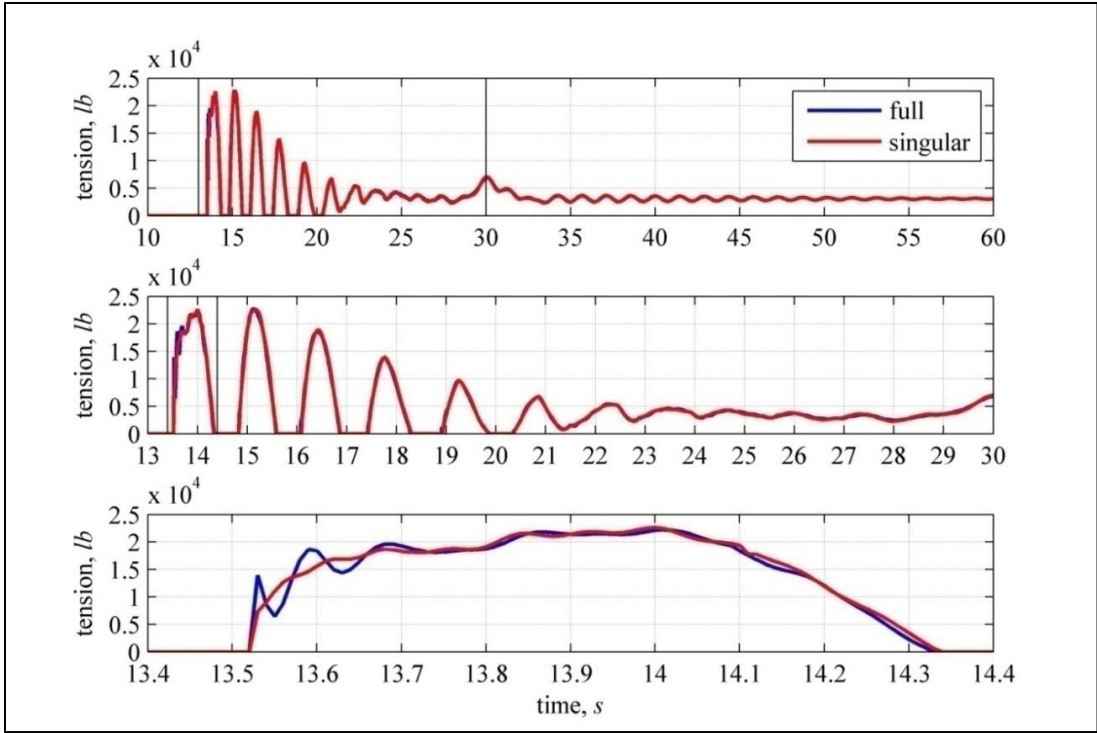


Fig. 3.26 Pad Abort 1 tension history of bridle 2

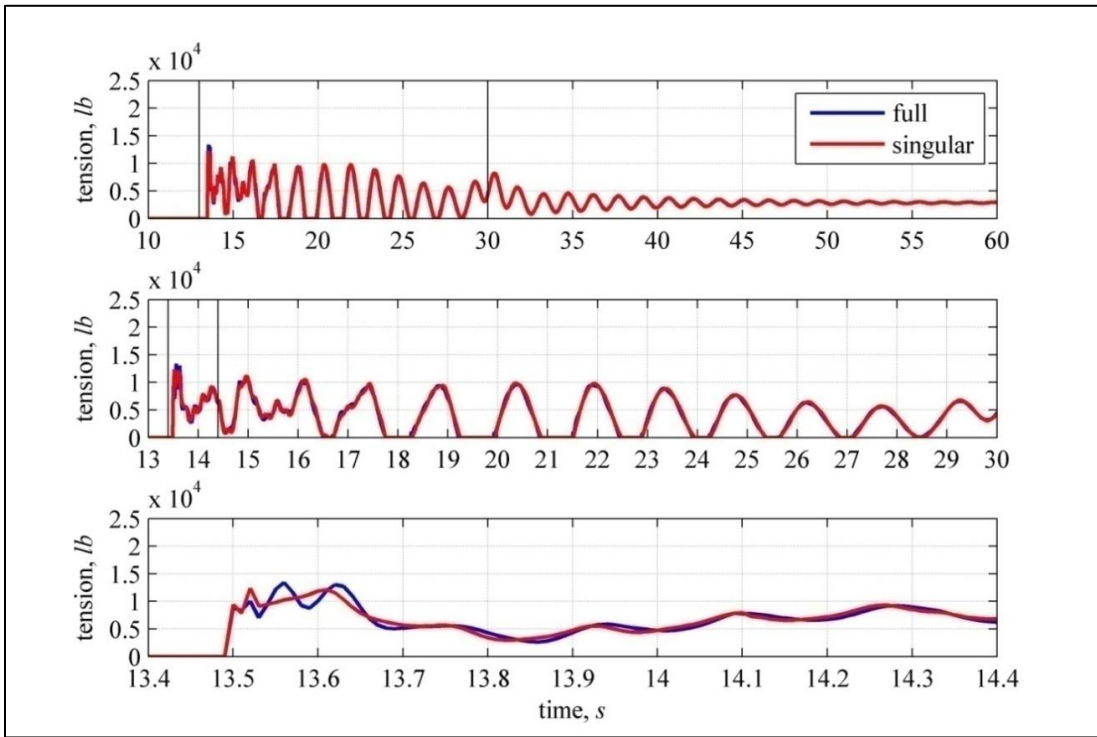


Fig. 3.27 Pad Abort 1 tension history of bridle 3

Line tensions from the singular perturbation method compare closely with the full solution even during periods of extreme slackness, indicated by the singular solution output matching in frequency, phase, and averaged tension values. The agreement is seen particularly in the long period oscillation of the tensions, and slightly less so in short period oscillations caused by approximations of the rapid motion of the confluence point. The agreement in tension is significantly improved from the MER test cases exploring slack cases, most likely due to the lower frequency and duration of the slackness. Many typical trajectory analyses would be engineered to avoid severe line slackness as well, so results from the CEV Pad Abort 1 scenario represent a better test bed for evaluating the overall utility and accuracy of the singular perturbation method. Additional plots comparing the output data, including riser tension, can be found in Appendix C.

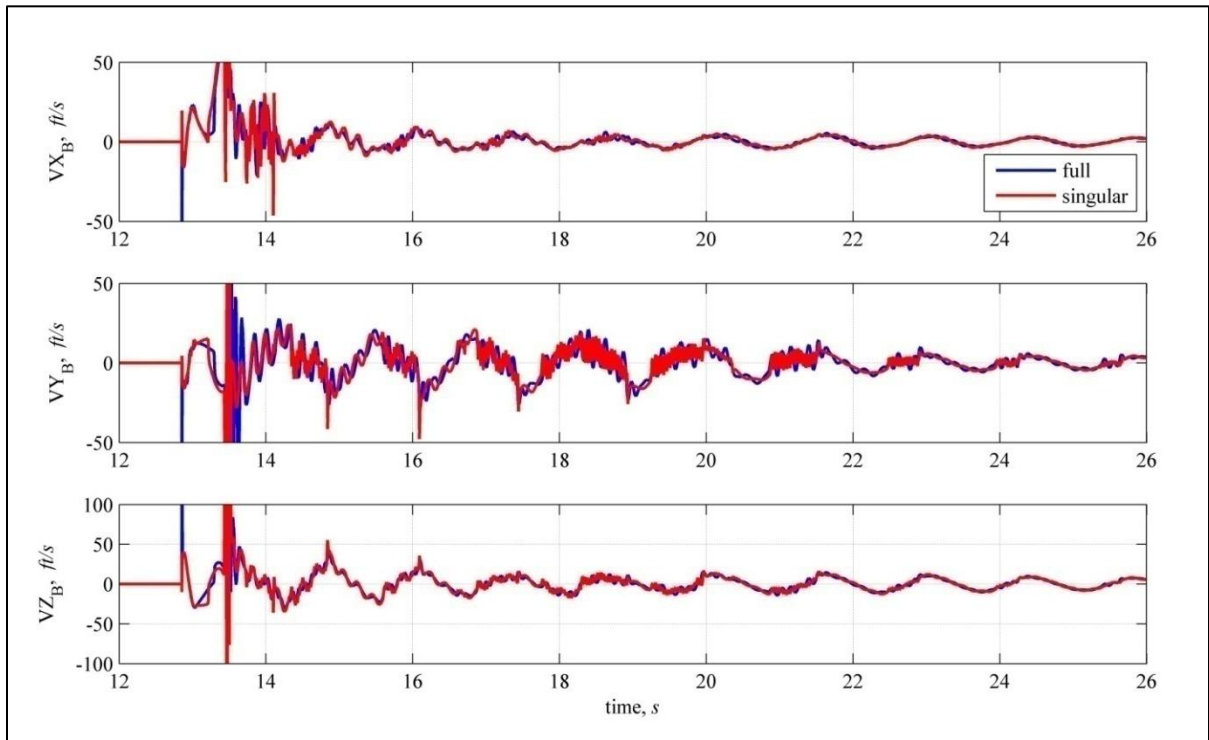


Fig. 3.28 Pad Abort 1 confluence point relative velocity (CEV body frame)

The calculated velocity of the confluence point in the singular perturbation solution indicates rapid, short period induced oscillations during slack instances. Figure 3.28 indicates less of such oscillation in the integrated results. This difference is attributed to the applied confluence damping force. Slack portions can be quickly identified by the thicker, high frequency behavior. Despite the increased deviation in the velocity, the approximate trend follows that of the full equation solution. This results in close agreement in the position of the confluence point. Portions later into the simulation are not plotted because of negligible difference in results once the confluence point has settled.

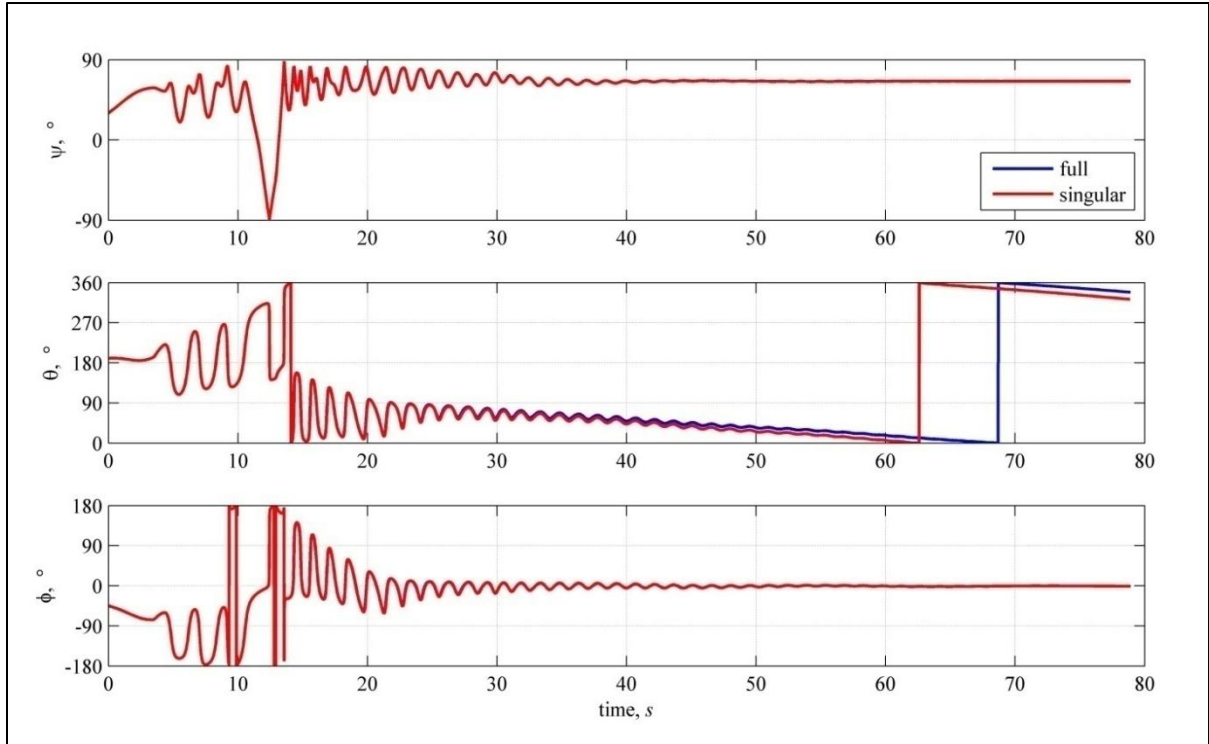


Fig. 3.29 Pad Abort 1 CEV Euler orientation angles

The orientation of the CEV capsule and the parachute are shown using Euler orientation angles. The orientation data from both solution sets agree over the initial portion of the analysis, with slight deviation later once the system has settled dynamically. Slight deviation in the capsule orientation is attributed to the use of confluence point damping during slack instances earlier in the simulation. The deviation has little effect on the orientation of the capsule, indicated by matching angle of attack and sideslip angles in Appendix C. The angular rates of the capsule are virtually identical between data sets.

3.3 Discussion

Generally speaking, the singular perturbation method for the MER and CEV test cases produces comparable results against the full equation of motion solution with mass applied at the confluence point, between twenty and one-hundred times the integration time step. The largest increases in time step are admittedly only permitted in the simplest cases in which the confluence mass experiences little high frequency motion. High time steps used with the singular perturbation method produce high frequency artifacts that worsen during periods of slackness and rapid confluence point motion. The test cases presented examine the robustness of the method in baseline conditions as well as rare occurrences of excessive line slackness and vehicle swinging. In cases where slackness is not encountered and no confluence damping is needed, the results are nearly identical. After the inclusion of confluence damping, discrepancies appear in the form of inertial position and orientation. The difference is tied directly to the amount of damping applied to the confluence point when propagating past instances of singularity.

Before the application of the condition number shown in the method, a constant confluence damping term was defined and often led to severe differences in results between data sets. The MER test cases 3 and 4 resulted in final lateral positions differing by up to 100 meters with the use of constant confluence damping. Use of the condition number allows variable application of confluence damping in varied amounts allowing as close to nominal a solution as possible. Though differences in long-term behavior of the system are observed after application of confluence damping, its necessity has been established in the theory section.

The singular perturbation method as presented has a great deal of versatility. Theoretically it may be used to abbreviate the equations of motion of any mass connected to significantly heavier bodies by any number of massless springs with damping. The method can be easily applied to an integrator by way of replacing the solution for the confluence velocity with Eq. (3.10). Results from

the method closely agree with the full solution for smaller confluence point masses, as the singular perturbation method provides the motion as though the connection point has no mass. Systems which experience severe slackness in the connecting lines will also show more deviation from the singular perturbation method. Inclusion of the restoring damping force on the connecting mass is essential to keep the solution from going unstable. Higher occurrence of slackness will result in greater deviations due to the stabilizing damping forces.

Other limitations found with the procedure dealt with systems which included extremely under-damped systems. A major characteristic of the singular perturbation method is the reliance upon damping values to solve for the inertial velocity of the confluence point. Low values of damping cause the system to become ill-conditioned, leading to rapidly diverging solutions for confluence velocity. In this case the analyst would be better suited with the equilibrium point solution⁷ which disregards damping values. Otherwise, the line damping must be increased until the singular perturbation solution converges.

4 Conclusions

Two new methods for predicting confluence point behavior in parachute multibody simulations have been presented. The goal behind developing the methods is to reduce processing requirements of these multibody simulations, in which the use of a confluence point can severely hamper analysis turnaround times. The dynamics of a system are more accurately represented with the use of a confluence point, offering substantial benefits with effective application of the methods. The two methods can be easily modified for generic systems that have any number of connection lines between multiple bodies and a single small confluence mass. The analytic method was developed and modeled in a simple fixed system, while the singular perturbation method was tested in various simple analyses on the MER capsule as well as a high-fidelity descent trajectory with the CEV pad abort mode.

Several conclusions can be drawn from the analyses on this complex and multi-faceted problem. Foremost, the past work in the equilibrium point solution as well as the presented results of the analytic method based upon it greatly assist in the understanding of how the confluence point behaves while in motion. The linearization of the confluence point equations of motion about the equilibrium point reveal approximate simple harmonic motion, heretofore unnoticed in the study of these types of models. Understanding the physical nature of the model is the most important step in devising such techniques to abbreviate the numerical stiffness within the system. Obstacles in using the analytic linearization in a full simulation are those of the equilibrium point solution, given that a Newton iterative solver is required to converge at every time step in the integration. Additional calculations within the analytic solution make it more computationally costly than the equilibrium point solution. These issues, as well as the fact that the equilibrium point solution already provides sufficient results (assuming convergence) made applying the analytic method within a trajectory integrator

unattractive. Creation of a new model which did not suffer the same non-convergence limitations was ultimately desired.

The singular perturbation method manages to bypass the problems of non-convergence while simultaneously handling interference from slack cases with minimal confluence point damping. Results from the comparisons show close agreement between results from the singular perturbation method and from full integration with mass applied at the confluence point. The integration time step was increased by 100 times for the MER analyses, and by 20 times for the CEV parachute simulation portion. Swinging motion is appropriately handled, as well as portions of high frequency motion generally seen in the initial stages of the simulations. The method is exceptionally strong in steady-state cases in which no slackness is experienced by the connecting lines. When slackness is an issue, the imposed confluence point damping force is applied in increasing amounts until the system is no longer ill-conditioned for each particular slack case. The metric for grading the system for ill-conditioning is determined by the user by way of a condition number. The differences in the results from the methods are a function of the frequency of slack cases experienced.

Other observations reveal the weakness of the singular perturbation method with the use of severely under-damped systems, for which the ill-conditioning of the problem disallows correct solution of inertial velocity. Systems which utilize no damping or very little damping would be required to use the equilibrium point solution, perhaps with methods to handle slack line cases similar to the singular perturbation method. Generally speaking, a majority of descent models incorporating a confluence mass would show turnaround time improvements from application of these methods, with similar predicted behavior.

References

¹Poole, L. R., and Huckins, E. K., "Evaluation of Massless Spring Modeling of Suspension Line Elasticity During the Parachute Unfurling Process," NASA TN D-6771, Feb 1972.

²Poole, L. R., "Computer Program for Investigating Effects of Nonlinear Suspension System Elastic Properties on Parachute Inflation Loads and Motions," NASA TM X-2592, Aug 1972.

³Whitlock, C.H., Poole, L. R., and Talay, A. T., "Postflight Simulation of Parachute Deployment Dynamics of Viking Qualification Flight Tests," NASA TN D-7415, Sep 1973.

⁴Doyle, G.R., and Burbick, J.W., "Users Manual: Dynamics of Two Bodies Connected by an Elastic Tether," Goodyear Aerospace Corp., GER-16047, Akron, Oh, April 1974.

⁵Raiszadeh, B., Queen E.M., "Partial Validation of Multibody Program to Optimize Simulated Trajectories (POST II) Parachute Simulation with Interacting Forces," NASA TM-2002-211634, April 2002.

⁶Raiszadeh, B., and Queen, E.M., "Mars Exploration Rover Terminal Descent Mission Modeling and Simulation," American Astronautical Society Paper 04-271, Dec 2004.

⁷Raiszadeh, B., "Multibody Parachute Flight Simulations for Planetary Entry Trajectories Using Equilibrium Points," *Advances in the Astronautical Sciences*, Vol. 114, Suppl.; 2003, pp. 903-914.

⁸Program to Optimize Simulated Trajectories: Volume II, Utilization Manual, prepared by: R.W. Powell, S.A. Striepe, P.N. Desai, P.V. Tartabini, E.M. Queen; NASA Langley Research Center, and by: G.L. Brauer, D.E. Cornick, D.W. Olson, F.M. Petersen, R. Stevenson, M.C. Engel, S.M. Marsh; Lockheed Martin Corporation, Version 1.1.1 .G, May 2000.

⁹Dedieu, J.D., and Tisseur, F., "Perturbation theory for homogeneous polynomial eigenvalue problems," *Linear Algebra and its Applications*, Vol. 358, 2003, pp. 71-94.

¹⁰Meyer, C.D., "Inverses of Sums and Sensitivity," *Matrix Analysis and Applied Linear Algebra*, 1st ed., Society for Industrial and Applied Mathematics, Philadelphia, PA, 2000, pp. 124-130.

Appendices

Appendix A – Linearized Equivalence Matrix Components

$$\bar{C} = \begin{bmatrix} \frac{\partial f_x}{\partial \dot{r}_{cx}} & \frac{\partial f_x}{\partial \dot{r}_{cy}} & \frac{\partial f_x}{\partial \dot{r}_{cz}} \\ \frac{\partial f_y}{\partial \dot{r}_{cx}} & \frac{\partial f_y}{\partial \dot{r}_{cy}} & \frac{\partial f_y}{\partial \dot{r}_{cz}} \\ \frac{\partial f_z}{\partial \dot{r}_{cx}} & \frac{\partial f_z}{\partial \dot{r}_{cy}} & \frac{\partial f_z}{\partial \dot{r}_{cz}} \end{bmatrix}_{r_c=r_{eq}} \quad \bar{K} = \begin{bmatrix} \frac{\partial f_x}{\partial r_{cx}} & \frac{\partial f_x}{\partial r_{cy}} & \frac{\partial f_x}{\partial r_{cz}} \\ \frac{\partial f_y}{\partial r_{cx}} & \frac{\partial f_y}{\partial r_{cy}} & \frac{\partial f_y}{\partial r_{cz}} \\ \frac{\partial f_z}{\partial r_{cx}} & \frac{\partial f_z}{\partial r_{cy}} & \frac{\partial f_z}{\partial r_{cz}} \end{bmatrix}_{r_c=r_{eq}}$$

$$\frac{\partial f_x}{\partial \dot{r}_{cx}} = \sum_{i=1}^4 C_i n_{ix}^2 \quad \frac{\partial f_y}{\partial \dot{r}_{cy}} = \sum_{i=1}^4 C_i n_{iy}^2 \quad \frac{\partial f_z}{\partial \dot{r}_{cz}} = \sum_{i=1}^4 C_i n_{iz}^2$$

$$\frac{\partial f_x}{\partial \dot{r}_{cy}} = \frac{\partial f_y}{\partial \dot{r}_{cx}} = \sum_{i=1}^4 C_i n_{ix} n_{iy} \quad \frac{\partial f_x}{\partial \dot{r}_{cz}} = \frac{\partial f_z}{\partial \dot{r}_{cx}} = \sum_{i=1}^4 C_i n_{ix} n_{iz} \quad \frac{\partial f_y}{\partial \dot{r}_{cz}} = \frac{\partial f_z}{\partial \dot{r}_{cy}} = \sum_{i=1}^4 C_i n_{iy} n_{iz}$$

$$\frac{\partial f_x}{\partial r_{cx}} = \sum_{i=1}^4 K_i \left\{ 1 + L_{0,i} \left[\frac{(r_{ix} - r_{cx})^2}{L_i^3} - \frac{1}{L_i} \right] \right\}$$

$$\frac{\partial f_y}{\partial r_{cy}} = \sum_{i=1}^4 K_i \left\{ 1 + L_{0,i} \left[\frac{(r_{iy} - r_{cy})^2}{L_i^3} - \frac{1}{L_i} \right] \right\}$$

$$\frac{\partial f_z}{\partial r_{cz}} = \sum_{i=1}^4 K_i \left\{ 1 + L_{0,i} \left[\frac{(r_{iz} - r_{cz})^2}{L_i^3} - \frac{1}{L_i} \right] \right\}$$

$$\frac{\partial f_x}{\partial r_{cy}} = \frac{\partial f_y}{\partial r_{cx}} = \sum_{i=1}^4 K_i \left\{ \frac{L_{0,i}}{L_i} (r_{ix} - r_{cx})(r_{iy} - r_{cy}) \right\}$$

$$\frac{\partial f_x}{\partial r_{cz}} = \frac{\partial f_z}{\partial r_{cx}} = \sum_{i=1}^4 K_i \left\{ \frac{L_{0,i}}{L_i} (r_{ix} - r_{cx})(r_{iz} - r_{cz}) \right\}$$

$$\frac{\partial f_y}{\partial r_{cz}} = \frac{\partial f_z}{\partial r_{cy}} = \sum_{i=1}^4 K_i \left\{ \frac{L_{0,i}}{L_i} (r_{iy} - r_{cy})(r_{iz} - r_{cz}) \right\}$$

Appendix B – Derivation of Equilibrium Point Inertial Velocity

The condition for equilibrium of tensions imparted by line stiffness is defined by

$$f_x = \sum_{i=1}^4 K_i n_{ix} (L_i - L_{0,i}) = \sum_{i=1}^4 K_i (r_{ix} - r_{cx}) \left(1 - \frac{L_{0,i}}{L_i}\right) = 0$$

$$f_y = \sum_{i=1}^4 K_i n_{iy} (L_i - L_{0,i}) = \sum_{i=1}^4 K_i (r_{iy} - r_{cy}) \left(1 - \frac{L_{0,i}}{L_i}\right) = 0$$

$$f_z = \sum_{i=1}^4 K_i n_{iz} (L_i - L_{0,i}) = \sum_{i=1}^4 K_i (r_{iz} - r_{cz}) \left(1 - \frac{L_{0,i}}{L_i}\right) = 0$$

Differentiation of the functions above with respect to the attachment point velocities provides the equilibrium point velocity.

$$\left(\frac{\partial f}{\partial r_c} \Big|_{r_c=r_{eq}} \right) \vec{r}_{eq} = \sum_{i=1}^4 \left(\frac{\partial f}{\partial r_i} \Big|_{r_c=r_{eq}} \vec{r}_i \right)$$

Expanding provides

$$\begin{bmatrix} \frac{\partial f_x}{\partial r_{cx}} & \frac{\partial f_x}{\partial r_{cy}} & \frac{\partial f_x}{\partial r_{cz}} \\ \frac{\partial f_y}{\partial r_{cx}} & \frac{\partial f_y}{\partial r_{cy}} & \frac{\partial f_y}{\partial r_{cz}} \\ \frac{\partial f_z}{\partial r_{cx}} & \frac{\partial f_z}{\partial r_{cy}} & \frac{\partial f_z}{\partial r_{cz}} \end{bmatrix}_{r_c=r_{eq}} \vec{r}_{eq} = \sum_{i=1}^4 \begin{bmatrix} \frac{\partial f_x}{\partial r_{ix}} & \frac{\partial f_x}{\partial r_{iy}} & \frac{\partial f_x}{\partial r_{iz}} \\ \frac{\partial f_y}{\partial r_{ix}} & \frac{\partial f_y}{\partial r_{iy}} & \frac{\partial f_y}{\partial r_{iz}} \\ \frac{\partial f_z}{\partial r_{ix}} & \frac{\partial f_z}{\partial r_{iy}} & \frac{\partial f_z}{\partial r_{iz}} \end{bmatrix}_{r_c=r_{eq}} \vec{r}_i$$

The partial derivative matrices are symmetric, and are defined as

$$\frac{\partial f_j}{\partial r_{cj}} = - \sum_{i=1}^4 \frac{\partial f_j}{\partial r_{ij}} = - \sum_{i=1}^4 K_i \left(\frac{L_{0,i} (r_{ij} - r_{cj})^2}{L_i^3} - \frac{L_{0,i}}{L_i} + 1 \right)$$

$$\frac{\partial f_j}{\partial r_{ck}} = - \sum_{i=1}^4 \frac{\partial f_j}{\partial r_{ik}} = - \sum_{i=1}^4 \frac{K_i L_{0,i} (r_{ij} - r_{cj}) (r_{ik} - r_{ck})}{L_i^3}$$

where j and k are the axes along which the partial is taken, and $j \neq k$. The equilibrium point velocity is then solved by multiplying both sides by the $\frac{\partial f}{\partial r_c}$ matrix inverse.

Appendix C – Additional PA1 Simulation Output Data

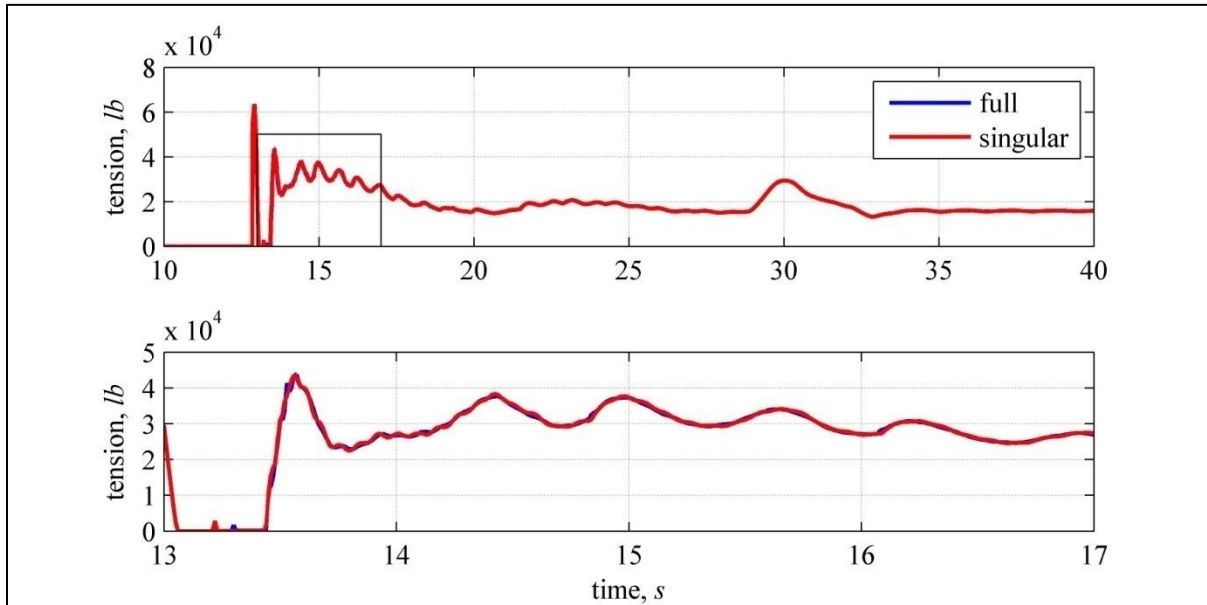


Fig 5.1 Tension history of riser

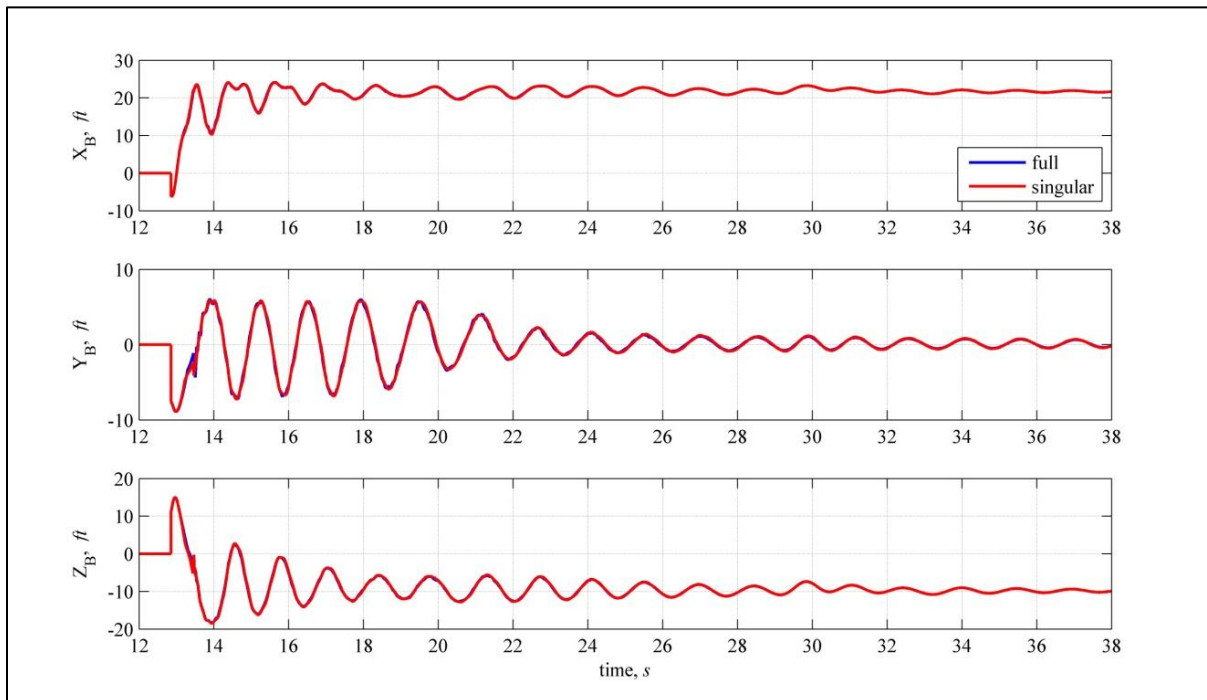


Fig 5.2 Confluence relative position in CEV body frame

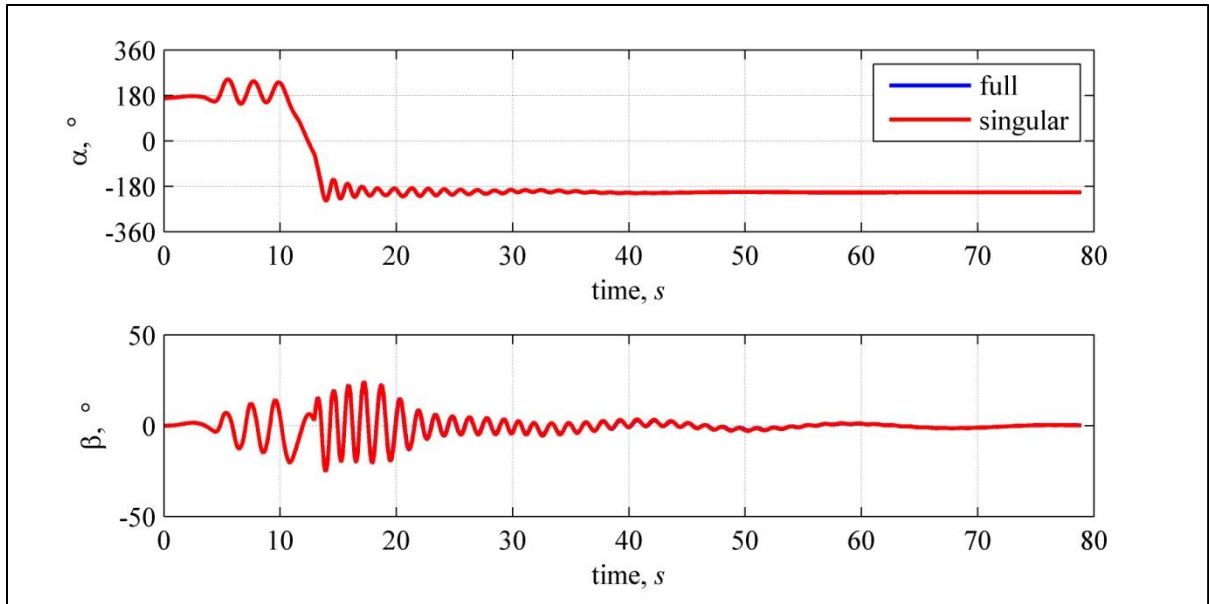


Fig 5.3 CEV angle of attack and sideslip angle

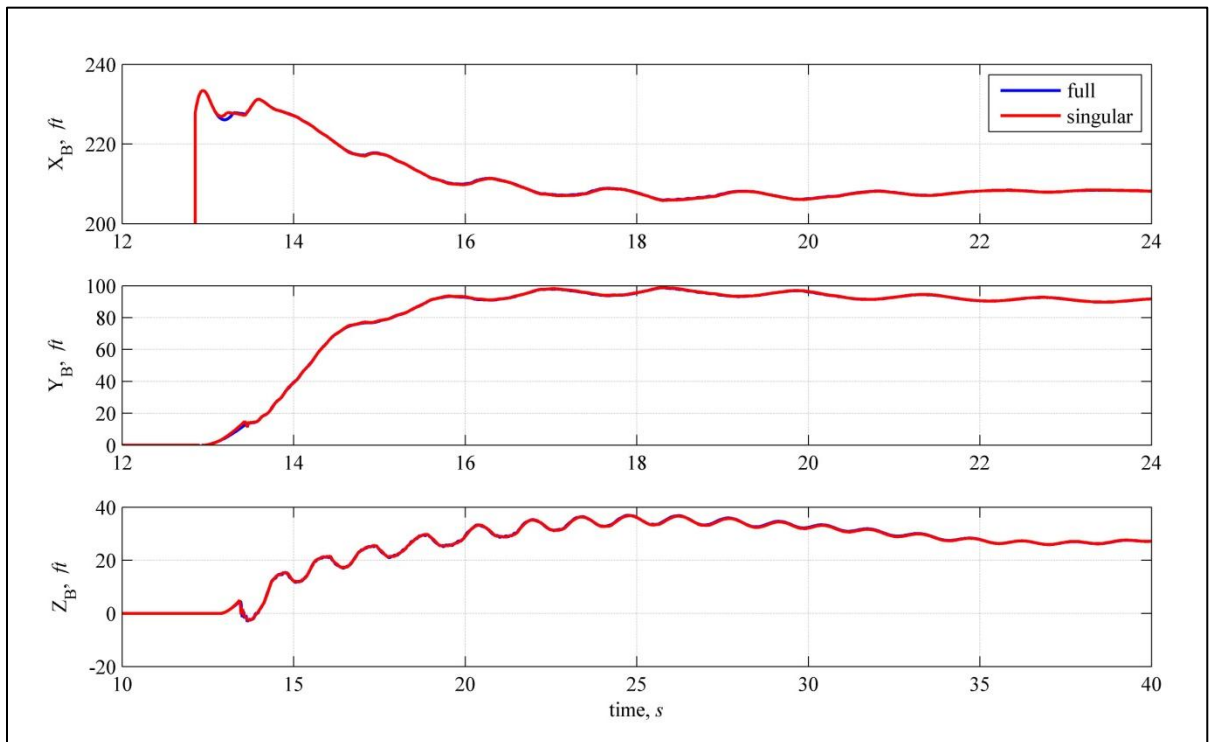


Fig 5.4 Parachute relative position in CEV body frame

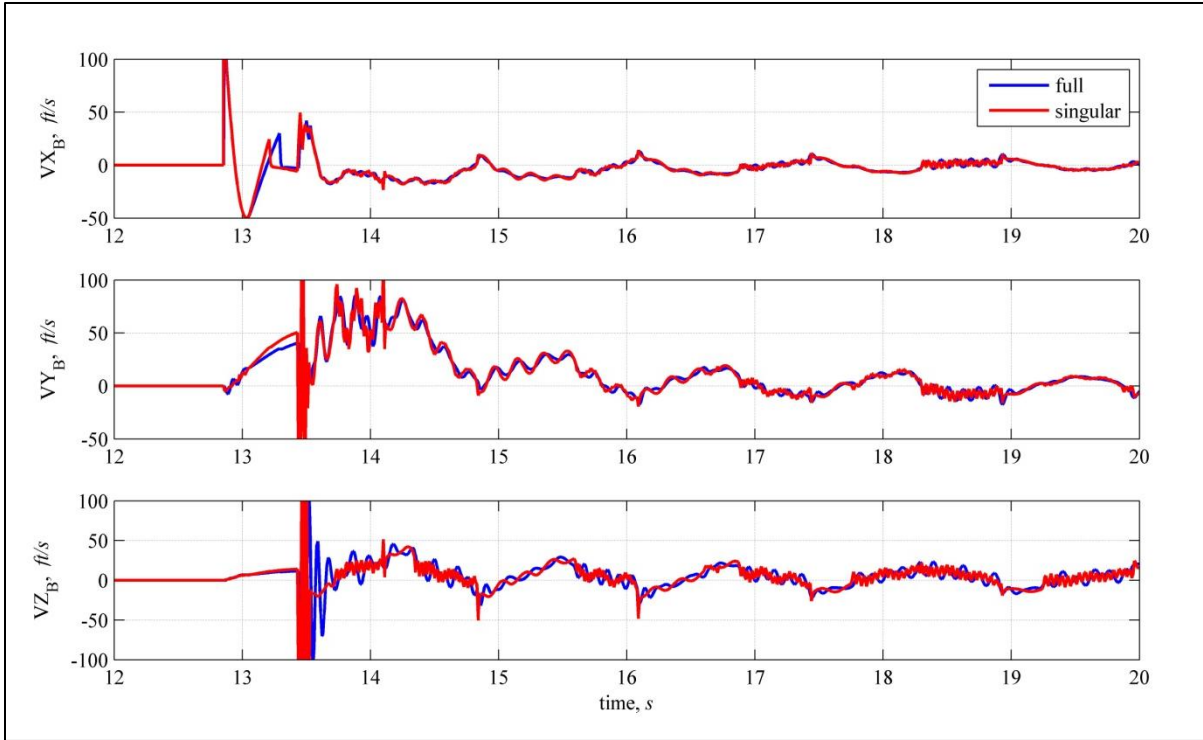


Fig 5.5 Parachute relative velocity in CEV body frame

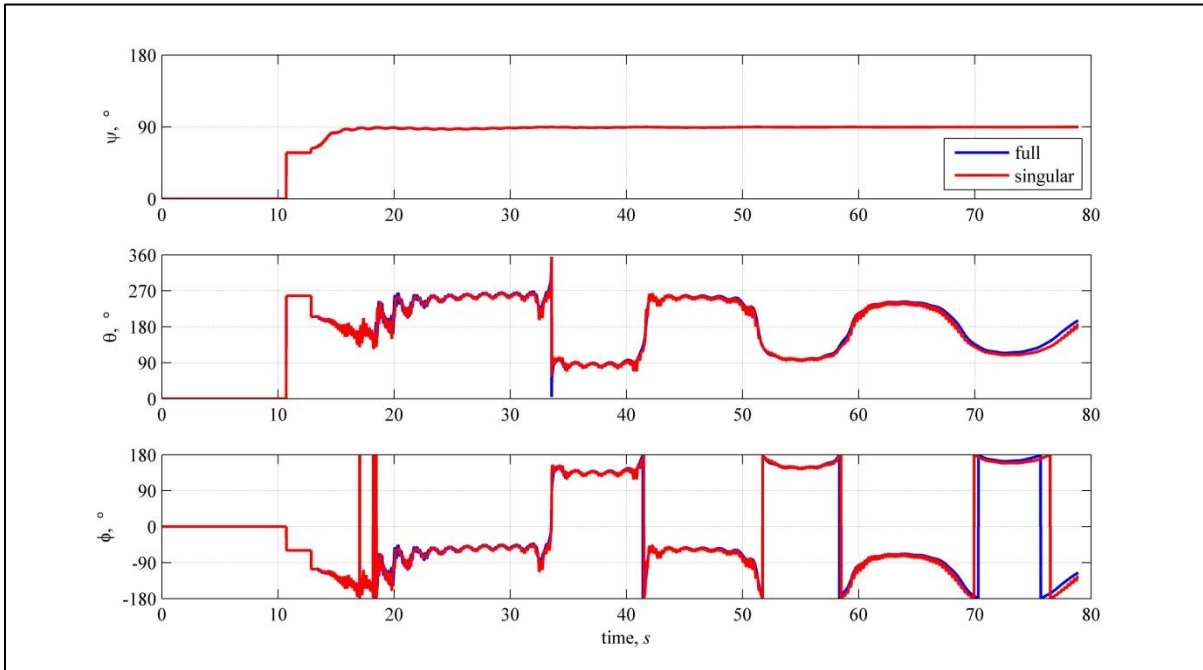


Fig 5.6 Parachute Euler orientation angles